The role of extraterrestrial particles in the formation of the ozone hole(*)

Part II: The action of extraterrestrial particles at ozone hole formation

T. C. Kerrigan(**) and J. Rosinski(***)

Visitors Department of Physics, University of Ferrara - Via Paradiso 12, 44100 Ferrara, Italy

Summary. — The object of this paper is to assess the possibility that particles of extraterrestrial origin play a significant role in the formation of the ozone hole. Preliminary analysis shows that air in the ozone layer over South Pole tends to be stable, saturated, and essentially particle-free just prior to ozone hole formation. Further, gas-phase reactions generally responsible for ozone loss in the atmosphere are unrelated to ozone hole formation. According to Part I of this paper, a massive influx of extraterrestrial particles invades the ozone layer over South Pole precisely at ozone hole formation. We hypothesize that ozone diffuses to the surfaces of these particles, where it is adsorbed and enters into a series of reactions leading to its net loss in the atmosphere. To test this hypothesis, we have constructed a mathematical model of this process. We have also identified principal features in ozone hole formation in field data for 1986. These include the start of ozone hole formation three weeks before sunrise, a spike in ozone concentration at sunrise, and cessation in ozone depletion before disintegration of the circumpolar vortex. Projections of the model are in good agreement with these features. To conclude, this analysis has developed strong evidence that the ozone hole is primarily a natural phenomenon caused by the depletion of ozone in reactions on the surfaces of extraterrestrial particles.

PACS 92.60 – Meteorology.
PACS 94.10 – Physics of the neutral atmosphere.
PACS 94.10.Fa – Atmospheric composition (atomic or molecular), chemical reactions and processes.
PACS 82.40.We – Atmospheric chemistry.

1. – Introduction

The object of this paper is to assess the possibility that particles of extraterrestrial origin play a significant role in the formation of the ozone hole. This assessment takes place in three steps.

The first is to estimate the concentration of extraterrestrial particles in the ozone layer over South Pole, Antarctica, during ozone hole formation. This estimate is based on an analysis of microscopic magnetic spherules collected in an extended program of atmospheric sampling. Spherules are shown to be of extraterrestrial origin and serve as markers for the larger class of less distinguished extraterrestrial particles. These particles settle to ground level as aggregates formed in a stratospheric ice crystal coalescence process. Specific spherule arrivals at ground level are strongly associated with apparent ozone depletion episodes during formation of the ozone hole. The origin of these spherules is a major stream of extraterrestrial particles independent of known meteor showers. The variability in its intensity from year to year corresponds to the variability in ozone depletion in the ozone hole itself. A quantitative theory based on this coalescence process has been used to project that the concentration of extraterrestrial particles at ozone hole formation lies between 500 and 2000 m^{-3}. In fact, this development constitutes Part I of this paper [1].
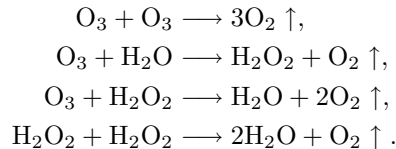
The second step (sect. **2**) is an analysis of the physics and chemistry of the ozone layer from sunset through winter over South Pole. This step is a key to understanding the state of the ozone layer when the ozone hole starts to form. Two features of the polar region simplify this analysis.

1) First, the poles are distinguished by a simplified radiation budget. Since the poles have just one day and one night per year, the evolution of ozone, which is largely driven by direct solar radiation, sees only semi-annual alternations of sunlight and shadow. Further, even for the sun at zenith, solar UV capable of dissociating O_2 is severely attenuated by the atmosphere above the ozone layer. The low angle of elevation of the sun above the horizon at the poles increases this attenuation exponentially. Since net production of ozone depends on photo-dissociation of O_2, net production in the ozone layer above South Pole is negligible.

2) Second, the circumpolar vortex tends to isolate the air of the polar region. During sunset and into winter, the general circulation in the polar region is characterized by a weak downdraft with infiltration at mid and upper altitudes in the ozone layer. As the vortex forms, the encircled air cools and stabilizes. Relative humidity increases until ice nucleation takes place on available particles. The formation of ice crystals keeps the water vapor density from rising much above saturation. Once formed, crystals settle out of the region under the influence of gravity. Air tends to be saturated and essentially particle free by mid winter.

A system of chemical reactions known to govern the evolution of ozone in the D region of the ionosphere has been adapted to the ozone layer. Predictions based on a mathematical model of this system generally agree with detailed ozone concentration measurements for the year 1986. The notable exception is the constant increase in ozone concentration just above the ozone layer throughout winter. Three possible explanations have been considered. Apparent inconsistencies in the data have left this issue unresolved.

The third step (sect. **3**) is an analysis of the formation of the ozone hole itself. A massive influx of extraterrestrial particles first arrives at the ozone layer over South

Pole three weeks before sunrise. These particles consist primarily of iron oxides and aluminum silicates. The water they acquire as they settle to the ozone layer forms a tightly bound monolayer through chemisorption. We hypothesize that ozone and water that subsequently adsorb on this monolayer form an uncondensed phase resembling a 2-dimensional gas. Constituents in this phase undergo the following reactions:

$$O_3 + O_3 \longrightarrow 3O_2 \uparrow,$$
$$O_3 + H_2O \longrightarrow H_2O_2 + O_2 \uparrow,$$
$$O_3 + H_2O_2 \longrightarrow H_2O + 2O_2 \uparrow,$$
$$H_2O_2 + H_2O_2 \longrightarrow 2H_2O + O_2 \uparrow.$$

The depletion of ozone by these reactions produces the ozone hole.

To test this hypothesis, we have identified features in field data for 1986 that a viable theory of ozone hole formation should explain. These include the start of ozone hole formation three weeks before sunrise, a spike in ozone concentration at sunrise, and cessation in ozone depletion before disintegration of the circumpolar vortex. We have also constructed a simple mathematical model that captures the essential features in this theory:

   i) the presence of extraterrestrial particles at ozone hole formation,

   ii) special conditioning of particle surfaces,

   iii) diffusion of atmospheric ozone and water to particle surfaces,

   iv) a system of chemical reactions at particle surfaces that result in ozone depletion,

   v) the role or adsorption/desorption in connecting atmospheric diffusion and surface chemistry.

Projections by the model are in good agreement with field measurements. We conclude that this analysis has developed strong evidence that the ozone hole is primarily a natural phenomenon caused by the depletion of ozone in reactions on the surfaces of extraterrestrial particles.
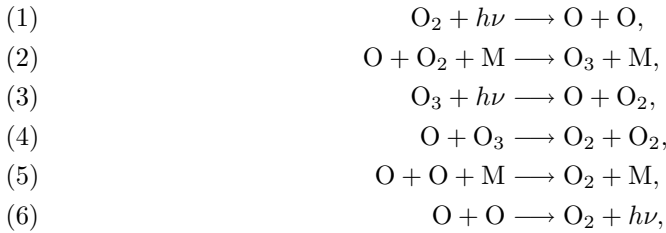

2. – Evolution of ozone-sunset through winter

The object of this section is to analyze the physics and chemistry of the ozone layer over South Pole prior to ozone hole formation. This analysis is a key to understanding the state of the ozone layer during ozone hole formation. Subsections **2**˙1 through **2**˙3 specify the system of rate equations for the evolution of [O] and [O$_3$] for sunset through winter. Subsections **2**˙4 and **2**˙5 derive the solution of this system. Subsections **2**˙6 and **2**˙7 compare predictions of this theory with detailed measurements taken in 1986. Finally, subsect. **2**˙8 considers the role of water in this theory. The theory will be extended in sect. **2** to include a mechanism through which extraterrestrial particles may actually produce the ozone hole.

TABLE I. – *Solar radiation wavelength intervals, corresponding contributions to extra-atmosphere dissociation coefficients j_1 and j_3 for O_2 and O_3, and optical depths of atmospheric penetration. Wavelengths shorter than 2424 Å contribute to j_1; longer wavelengths contribute to j_3.*

	Wavelength interval (Å)	Dissociation coefficient (s^{-1})	Optical depth (km)
Schumann-Runge continuum	1300–1750	6×10^{-6}	110
Schumann-Runge	1750–1850	10^{-8}	100
Absorption bands	1900–2000	10^{-9}	60
Herzberg continuum	2000–2424	1.5×10^{-9}	40
Hartley continuum	2424–2900	9.4×10^{-3}	40
Huggins bands	3000–3500	3.7×10^{-4}	–

2·1. *Rate equations.* – The object of this section is to specify the form of the rate equations for the evolution of [O] and [O_3] in the ozone layer. The following reactions govern this evolution at altitudes less than $100 \, km$ in the D region of the ionosphere [2]:

$$(1) \qquad O_2 + h\nu \longrightarrow O + O,$$

$$(2) \qquad O + O_2 + M \longrightarrow O_3 + M,$$

$$(3) \qquad O_3 + h\nu \longrightarrow O + O_2,$$

$$(4) \qquad O + O_3 \longrightarrow O_2 + O_2,$$

$$(5) \qquad O + O + M \longrightarrow O_2 + M,$$

$$(6) \qquad O + O \longrightarrow O_2 + h\nu,$$

$h\nu$ denotes a photon absorbed in the dissociative reactions (1) and (3), and a photon emitted in the associative reaction (6) M denotes a third body required to carry off energy in the three-body reactions (2) and (5).

The rate equations for [O] and [O_3] corresponding to this system are

$$(7) \qquad \frac{d[O]}{dt} = 2j_1[O_2] - \alpha_2[O_2][M][O] + j_3[O_3] - \alpha_4[O_3][O] - 2\alpha_5[M][O]^2 - 2\alpha_6[O]^2,$$

$$(8) \qquad \frac{d[O_3]}{dt} = \alpha_2[O_2][M][O] - j_3[O_3] - \alpha_4[O_3][O].$$

j_1 and j_3 denote radiative dissociation coefficients; α_2, α_4, α_5, and α_6 denote reaction rate coefficients. Numerical estimates of these coefficients for the ozone layer are developed in subsects. **2·2** and **2·3**.

2·2. *Dissociation coefficients.* – The object of this section is to estimate the contributions to j_1 and j_3 from various solar radiation wavelength intervals. Table I provides estimates of these contributions at the top of the atmosphere and the corresponding optical depths of penetration [2].

The contribution for any given interval depends on altitude of observation, angle of elevation of the sun above the horizon, and composition of the intervening atmosphere. Let $j(z)$ denote dissociation coefficient as a function of altitude for any given wavelength

TABLE II. – *Estimated contributions to radiative dissociation coefficients j_1 and j_3 from six solar radiation wavelength intervals at three altitudes. Wavelengths shorter than 2424 Å contribute to j_1; longer wavelengths contribute to j_3.*

	Wavelength interval (Å)	Dissociation coefficient (s^{-1})		
		14 km	19 km	24 km
Schumann-Runge continuum	1300–1750	0	0	0
Schumann-Runge	1750–1850	0	0	0
Absorption bands	1900–2000	2.7×10^{-88}	2.2×10^{-54}	4.2×10^{-35}
Herzberg continuum	2000–2424	9.5×10^{-18}	3.3×10^{-14}	3.4×10^{-12}
Hartley continuum	2424–2900	1.1×10^{-6}	1.5×10^{-6}	1.1×10^{-5}
Huggins bands	3000–3500	$< 3.7 \times 10^{-4}$	$< 3.7 \times 10^{-4}$	$< 3.7 \times 10^{-4}$

interval. For the sun at zenith, the relative rate of change of j with altitude is proportional to number density of interactive constituents [3]:

$$\frac{1}{j}\frac{\mathrm{d}j}{\mathrm{d}z} \propto n.$$

The solution of this equation is

$$j(z) = j(\infty)\exp\left[-c\int_z^\infty n\,\mathrm{d}z\right],$$

for proportionality constant c. This expression has been used to estimate contributions to j_1 and j_3 near the ozone layer. To satisfactory approximation, intervals with wavelengths shorter than 2424 Å contribute to j_1; intervals with longer wavelengths contribute to j_3. We have assumed $n \equiv [O_2]$ in estimating j_1 and $n \equiv [O_3]$ in estimating j_3. We have also assumed standard profiles for $[O_2]$ and $[O_3]$ [4]. Optical depths given in table I have been used to evaluate c for each wavelength interval.

Estimates of contributions to j_1 and j_3 are given in table II. Contributions to j_1 in the Schumann-Runge Continuum and Absorption Bands are virtually zero. The contribution in the Herzberg Continuum at 19 km is diminished by a factor of 10^{-5} from its extra-atmosphere value.

The estimates in table II take the sun to be at zenith. However, the maximum angle of elevation the sun makes with the horizon in the 30-day interval before sunset at South Pole is less than 11° (Appendix A). This angle corresponds to an increase in atmospheric mass traversed by solar radiation by a factor of at least 5. To satisfactory approximation, the estimate of $j(z)$ depends on an increase in atmospheric mass by a factor of "elev" according to

$$j(z) = j(\infty) \cdot \left(\exp\left[-\int_z^\infty n\,\mathrm{d}z\right]\right)^{\text{elev}},$$

where the integral is computed for the sun at zenith. When the entries in table II are revised to account for elev ≈ 5, all contributions to j_1 are virtually zero.

2`3. *Reaction rate coefficients*. – Values of the reaction rate coefficients α_2, α_4, α_5, and α_6 have been obtained for temperature $25\,°\text{C}$ [2]. However, temperatures of interest in this analysis range between -90 and $-40\,°\text{C}$. Values of these coefficients for temperature in this range have been extrapolated using elementary kinetic theory [5]. The theory takes the reaction rate for a gas-phase chemical reaction to be the product of two factors. The first is the collision rate for the reacting species. The second is an effective Boltzmann factor that accounts for a kinetic energy threshold the colliding species must exceed to bond chemically.

In particular, for reactions involving two molecules of species A and B, the reaction rate coefficient has the form

$$\alpha_{\text{AB}}(T) = \sigma_{\text{AB}} \cdot v_{\text{AB}}(T) \cdot \exp\left[-E_{\text{AB}}/RT\right],$$

where

$\quad\alpha_{\text{AB}}$ is the reaction rate coefficient (cm^3/s),

$\quad T$ is the temperature (K),

$\quad\sigma_{\text{AB}}$ is the collision cross-section for species A and B (cm^2),

$\quad v_{\text{AB}}$ is the relative velocity of species A and B (cm/s),

$\quad E_{\text{AB}}$ is the reaction energy threshold (J/mol),

$\quad R$ is the gas constant, $8.3144\,\text{J/K/mol}$.

The value of $\alpha_{\text{AB}}(T_0)$ at $T_0 = 25\,°\text{C}$ is used to estimate E_{AB}:

$$E_{\text{AB}} = -RT_0 \cdot \ln\left(\frac{\alpha_{\text{AB}}(T_0)}{\sigma_{\text{AB}} \cdot v_{\text{AB}}(T_0)}\right).$$

Note that if $\text{A} \equiv \text{B}$, the reaction rate must be discounted by a factor of $1/2$ to avoid double counting introduced by symmetry.

The reaction rate coefficient for reactions involving three molecules A, B, and M is also the product of the collision rate and the corresponding Boltzmann factor. A simple geometric argument provides the following estimate for the three-body collision rate:

$$\frac{4}{3}\pi^2\left(r_{\text{A}} + r_{\text{B}}\right)^3 r_{\text{M}}^2 v_{\text{M}}[\text{A}][\text{B}][\text{M}],$$

where r denotes effective radius and v denotes mean velocity. Then reaction rate coefficient has the form

$$\alpha_{\text{ABM}}(T) = \frac{4}{3}\pi^3\left(r_{\text{A}} + r_{\text{B}}\right)^3 r_{\text{M}}^2 v_{\text{M}}(T) \cdot \exp\left[-\frac{E_{\text{ABM}}}{RT}\right],$$

where

$$E_{\text{ABM}} = -RT_0 \cdot \ln\left(\frac{\alpha_{\text{ABM}}(T_0)}{(4/3)\pi^2\left(r_{\text{A}} + r_{\text{B}}\right)^3 r_{\text{M}} v_{\text{M}}(T_0)}\right).$$

M denotes air in this case (O_2 or N_2). This estimate for α_{ABM} was derived under the assumption that A, B, and M are distinct. Otherwise, the reaction rate coefficient must be discounted as in the two-body collision theory to avoid overcounting induced by symmetry.

Application of this theory yields the following general expressions:

$$\alpha_2(T) = 1.25 \times 10^{-32} \sqrt{\frac{T}{298}} \cdot \exp\left[-\frac{9300}{RT}\right],$$

$$\alpha_4(T) = 3.37 \times 10^{-10} \sqrt{\frac{T}{298}} \cdot \exp\left[-\frac{23000}{RT}\right],$$

$$\alpha_5(T) = 2.92 \times 10^{-33} \sqrt{\frac{T}{298}} \cdot \exp\left[-\frac{60}{RT}\right],$$

$$\alpha_6(T) = 1.11 \times 10^{-10} \sqrt{\frac{T}{298}} \cdot \exp\left[-\frac{36000}{RT}\right].$$

2˙4. *System solution—short term.* – The object of subsects. **2˙**4 and **2˙**5 is to solve eqs. (7) and (8) for the evolution of [O] and [O_3] in the ozone layer over South Pole prior to ozone hole formation. In this section, we eliminate terms in these equations that have negligible effect on the short-term evolution of [O] and [O_3]. Solution of the simplified system shows that [O] and [O_3] reach quasi-equilibrium within seconds. This result will enable us to eliminate [O] from explicit consideration in assessing the evolution of [O_3] on a time scale of days or weeks.

To evaluate the relative influence of the j_1 and j_3 terms in eq. (7), we evaluate their ratio with values of dissociation coefficients taken from tables I and II, [O_3] = 2.0 PPM(Air), and elev = 5. Then, $2j_1[O_2]/j_3[O_3] < 6 \times 10^{-15}$ for all three altitudes. Thus, we omit the j_1 term from eq. (7).

Estimates of typical values for the reaction rates in eqs. (7) and (8) are given in table III. Altitude was taken to be 19 km, the altitude of maximum ozone concentration, and temperatures were taken to be -45 and $-90\,°$C, the extremes at sunset and sunrise. In view of the uncertainty in [O], each term was evaluated for various values of the ratio [O]/[O_3]. According to table III, the reaction rate corresponding to α_2 is at least three orders of magnitude larger than the reaction rates corresponding to α_4, α_5, and α_6. Thus, we may omit the α_4, α_5, and α_6 terms from eqs. (7) and (8).

The short-term evolution of [O] and [O_3] is governed by the reduced system of equations

$$(9) \qquad \frac{\mathrm{d}[O]}{\mathrm{d}t} = -\bigl(\alpha_2[O_2]\bigl[M\bigr]\bigr) \cdot [O] + (j_3) \cdot [O_3],$$

$$(10) \qquad \frac{\mathrm{d}[O_3]}{\mathrm{d}t} = \bigl(\alpha_2[O_2][M]\bigr) \cdot [O] - (j_3) \cdot [O_3].$$

Given values $[O](t_0)$ and $[O_3](t_0)$ at some initial time t_0, and taking j_3 to be essentially constant over the relatively short time interval of interest, then the solution of this system

TABLE III. – *Estimates of reaction rates for eqs.* (7) *and* (8) *at* 19 km *altitude for two temperatures and four values of the ratio* [O]/[O$_3$].

[O]/[O$_3$]:	10^{-6}	10^{-4}	10^{-2}	10^{0}
$T = -45\,^\circ$C				
$\alpha_2[O_2][M][O]$:	2.8×10^{7}	2.8×10^{9}	2.8×10^{11}	2.8×10^{13}
$\alpha_4[O_3][O]$:	1.3×10^{4}	1.3×10^{6}	1.3×10^{8}	1.3×10^{10}
$2\alpha_5[M][O]^2$:	3.2×10^{-2}	3.2×10^{2}	3.2×10^{6}	3.2×10^{10}
$2\alpha_6[O]^2$:	7.7×10^{-6}	7.7×10^{-2}	7.7×10^{2}	7.7×10^{6}
$T = -90\,^\circ$C				
$\alpha_2[O_2][M][O]$:	7.4×10^{6}	7.4×10^{8}	7.4×10^{10}	7.4×10^{12}
$\alpha_4[O_3][O]$:	5.9×10^{2}	5.9×10^{4}	5.9×10^{6}	5.9×10^{8}
$2\alpha_5[M][O]^2$:	2.8×10^{-2}	2.8×10^{2}	2.8×10^{6}	2.8×10^{10}
$2\alpha_6[O]^2$:	6.2×10^{-8}	6.2×10^{-4}	6.2×10^{0}	6.2×10^{4}

is

$$[O_3](t) = [O](t_0) \cdot \exp\left[-\left(\alpha_2 \cdot [O_2] \cdot [M] + j_3\right) \cdot (t - t_0)\right) +$$

$$+ \frac{\left(\alpha_2 \cdot [O_2] \cdot [M]\right) \cdot \left([O](t_0) + [O_3](t_0)\right)}{\alpha_2 \cdot [O_2] \cdot [M] + j_3} \cdot$$

$$\cdot \left(1 - \exp\left[-\left(\alpha_2 \cdot [O_2] \cdot [M] + j_3\right) \cdot (t - t_0)\right)\right),$$

where $[O](t) + [O_3](t) = [O](t_0) + [O_3](t_0)$. The asymptotic values for $[O_3]$ and $[O]$ are given by

$$[O_3](\infty) = \frac{\alpha_2[O_2][M]}{\alpha_2[O_2][M] + j_3} \cdot \left([O](t_0) + [O_3](t_0)\right),$$

and

$$[O](\infty) = \frac{j_3}{\alpha_2[O_2][M] + j_3} \cdot \left([O](t_0) + [O_3](t_0)\right).$$

The relation between $[O_3]$ and $[O]$ at quasi-equilibrium is obtained by taking the ratio of these expressions:

(11) $$[O] \approx \frac{j_3}{\alpha_2[O_2][M]}[O_3].$$

Relaxation time $t_{1/2}$, the time for the variables $[O]$ and $[O_3]$ to reach the midpoint between their initial and asymptotic values, gauges the time for this system to approach quasi-equilibrium. $t_{1/2}$ satisfies $\exp[-(\alpha_2[O_2][M] + j_3)t_{1/2}] = 1/2$. Thus,

$$t_{1/2} = \frac{\ln(2)}{\alpha_2[O_2][M] + j_3}.$$

TABLE IV. – *Relaxation times, ratios of asymptotic number densities, expected lifetimes for* O *and* O_3 *molecules, and relative decreases in* $[O_3]$ *over a 30-day interval for temperatures* $= -45$ *and* -90 °C.

	-45 °C	-90 °C
$t_{1/2}$	0.074 s	0.28 s
$[O](\infty)/[O_3](\infty)$	1.03×10^{-5}	2.8×10^{-5}
$t_{[O]}$	0.11 s	0.40 s
$t_{[O_3]}$	2.8 h	2.8 h
$[O_3](30 \text{ days})/[O_3](0 \text{ days})$	0.89	0.98

Finally, note that the expected lifetime for any given molecule is the reciprocal of the corresponding reaction rate. Thus, the expected lifetimes for O and O_3 are given by $t_{[O_3]} = 1/j_3$, and $t_{[O]} = 1/\alpha_2[O_2][M]$. Table IV contains estimates of $[O](\infty)/[O_3](\infty), t_{1/2}, t_{[O]},$ and $t_{[O_3]}$ for $j_3 = 10^{-4}$, altitude 19 km, and temperatures -45 and -90 °C.

To summarize, a quasi-equilibrium between the O and O_3 populations is established within seconds. At quasi-equilibrium, $[O]/[O_3] < 10^{-4}$. The expected lifetime of an O_3 molecule is greater than two hours. The molecule dissociates according to reaction (3). The expected lifetime of a liberated O atom is less than one second. The O atom recombines with an O_2 molecule to form an O_3 molecule according to reaction (2), and the cycle repeats.

2˙5. *System solution—long term.* – The object of this section is to determine the evolution of [O] and $[O_3]$ in the long term. Approximations developed in subsect. **2˙4** lead to reductions of eqs. (7) and (8) that can be solved exactly.

First, recall that $2j_1[O_3]$ is negligible over South Pole within 30 days of sunset. Next, note that the short relaxation time for the system of eqs. (9) and (10) implies the quasi-equilibrium constraint (11). Finally, note that $[O](\infty)/[O_3](\infty) \approx 10^{-5}$ (table IV). In this case, $\alpha_4[O_3][O]$ dominates $2\alpha_5[M][O]^2$ and $2\alpha_6[O]^2$. With these approximations, eq. (8) takes the form

$$(12) \qquad \frac{\mathrm{d}[O_3]}{\mathrm{d}t} \approx -\alpha_4[O_3][O] = -\frac{j_3\alpha_4}{\alpha_2[O_2][M]}[O_3]^2.$$

The solution is given by

$$[O_3](t) = \frac{[O_3](t_0)}{1 + (\alpha_4[O_3](t_0)/\alpha_2[O_2][M]) \displaystyle\int_{t_0}^{t} j_3 \, \mathrm{d}t}.$$

This expression has been used to estimate $[O_3](t)/[O_3](t_0)$ for $t - t_0 = 30$ days, $j_3 = 10^{-4}$(const), $[O_3](t_0) = 4.0 \times 10^{-6} \cdot [M]$ (*i.e.*, 4 PPM), altitude 19 km, and temperatures -45 and -90 °C. The results appear in table IV. $[O_3]$ declines by 11% at -45 °C and by 2% at -90 °C over this 30-day period. Recall that $j_3 = 10^{-4}$ is a generous upper bound so these estimates should prove to be high.

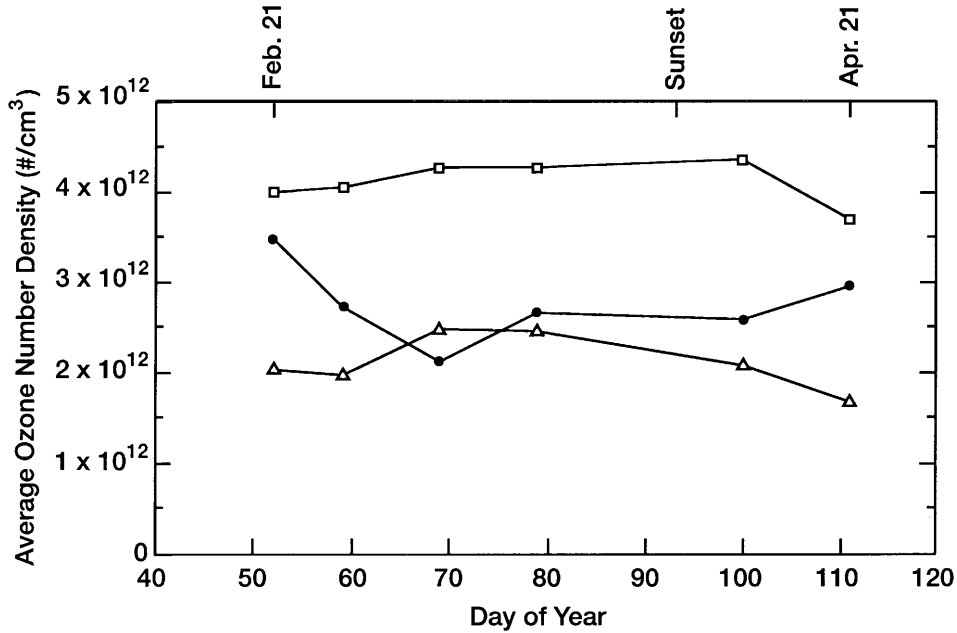To summarize, expectations set by this theory for the ozone layer over South Pole near sunset:

Fig. 1. – Average ozone number density *vs.* day of year near sunset ($\sim$ April 3) for three 5 km altitude intervals over South Pole, 1986 ($\triangle$ 14 km, $\square$ 19 km, $\bullet$ 24 km).

i) Direct UV capable of dissociating O_2 does not effectively penetrate to the ozone layer. Thus, there is virtually no net production of O_3 according to the reactions (1) and (2).

ii) The O and O_3 populations evolve in concert according to reactions (2) and (3). At quasi-equilibrium, the lifetime of an O atom is at least four orders of magnitude shorter than the lifetime of an O_3 molecule. Equivalently, $[O]/[O_3] < 10^{-4}$. In general, $[O]$ and $[O_3]$ are related by constraint (11). Deviations from this relation are suppressed within seconds.

iii) In the long term, $[O_3]$ evolves according to eq. (12). Thus, $[O_3]$ decreases at a rate proportional to $[O_3]^2$ and j_3. The decrease in $[O_3]$ is less than 12% in the month just prior to sunset. Ozone loss by this mechanism is about five times slower at $-90\,°C$ than at $-45\,°C$, *i.e.* five times slower at sunrise than at sunset. Finally, $j_3 = 0$ after sunset, so $[O_3]$ should be constant during winter.

2˙6. *Data analysis—sunset.* – The data presented in this section is recast ozone partial pressure data taken over South Pole for the year 1986 [6]. Figure 1 shows average number density for ozone ($\#/cm^3$) near sunset (Appendix A) in three 5 km altitude intervals. The graphs are labeled by the interval midpoints: 14, 19, and 24 km. Taken together, these intervals contain most of the ozone in the ozone layer.

The variations in $[O_3]$ at all three altitudes shown in fig. 1 conflict with the expectations set by the theory developed in subsects. **2˙1** through **2˙5**:

i) $[O_3]$ in the 24 km interval falls 38% between day 52 and day 69. A decline is predicted by the theory but this rate is much larger than the corresponding estimate
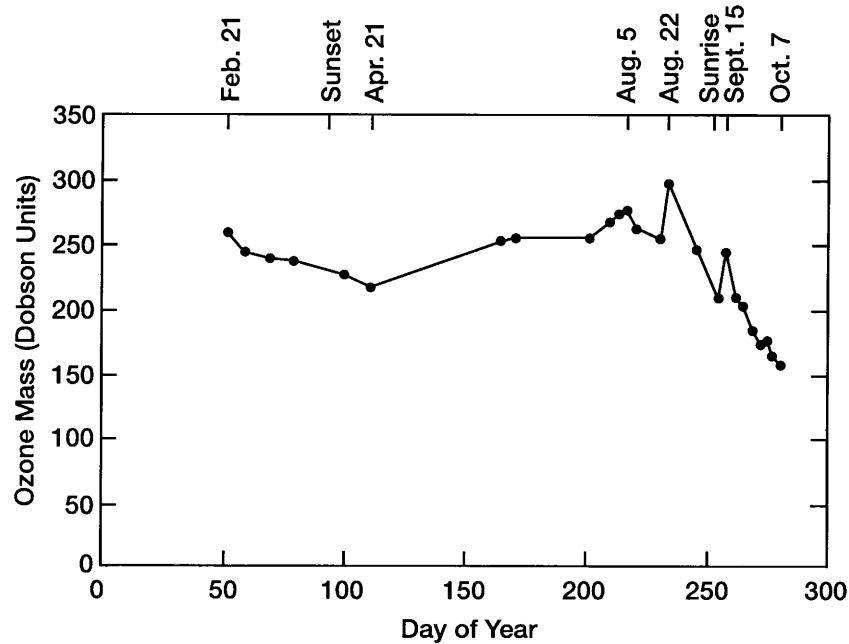
Fig. 2. – Total ozone mass *vs.* day of year in a standard column over South Pole, 1986.

given in table IV. [O$_3$] then rises 39% between day 69 and day 111. This period straddles sunset ($\sim$ April 3), so the increase in [O$_3$] occurs partly in sunlight, where the theory predicts a decrease, and partly on darkness, where the theory predicts no change.

ii) [O$_3$] in the 19 km interval rises 9% between day 52 and day 100. This period also straddles sunset. In fact, the increases before and after sunset are comparable, which suggests that the cause is independent of sunlight. [O$_3$] then falls 15% between day 100 and day 111, well after sunset, when the theory predicts no change.

iii) [O$_3$] in the 14 km interval increases abruptly by 25% between day 59 and day 69, and then decreases by 33% at an increasing rate between day 69 and day 111. The rate of decrease is evidently unaffected by sunset, which suggests that the cause of the decrease is independent of sunlight at this altitude also.

The easiest explanation for these variations is found in fig. 2, which shows ozone mass *vs.* day of year. Ozone mass is taken to be the total mass of ozone in a vertical column of unit cross-sectional area extending from the bottom of the atmosphere to the top (Dobson units). This quantity declines 16% at a relatively constant rate between days 52 and 111.

The sum of O$_3$ concentrations for any given day represented in fig. 1 is proportional to the total mass of ozone in the vertical column from 11.5 to 26.5 km. The trend in this sum conforms to the trend in total ozone shown in fig. 2 for days 52 to 111. The simplicity of this trend suggests that fluctuations are produced by atmospheric transport rather than complex chemical processes of ozone creation and destruction. In particular,
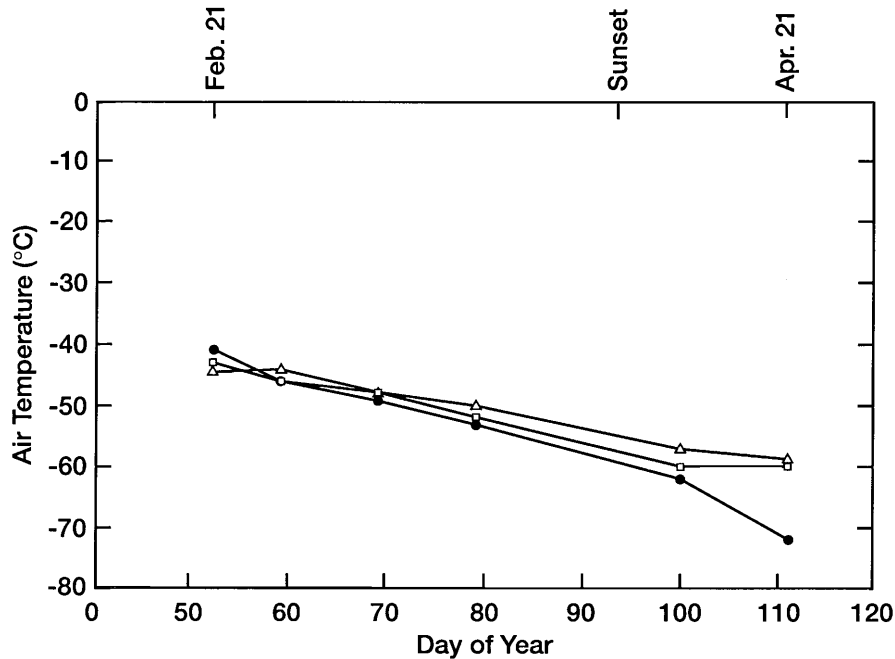
Fig. 3. – Air temperature *vs.* day of year near sunset ($\sim$ April 3) at three altitudes over South Pole, 1986 ($\triangle$ 14 km, $\square$ 19 km, $\bullet$ 24 km).

i) Atmospheric cooling near sunset shown in fig. 3 is associated with the infiltration and descent of air from outside the polar region. This infiltration includes air of relatively low ozone concentration from above the level of the ozone layer. Fluctuations in measured ozone concentrations occur until the vortex fully forms and the encircled air stabilizes [6]. Figures 1 and 2 suggest that this process completes after day 111. Thus, transport provides the easiest explanation for not just the fluctuations but also the trend itself.

ii) The apparent indifference of the evolution of ozone to sunset shown in both fig. 1 and fig. 2 indicates that ozone depletion via reactions (3) and (4) is insignificant. Not only is the magnitude of j_3 insufficient to produce discernable ozone depletion but evidence of the effect of any other photochemical depletion mechanism is also absent.

$2\dot{}7$. *Data analysis—winter*. – Contrary to expectations, fig. 2 shows a 37% increase in the total mass of ozone over South Pole between days 111 and 234. To analyze this increase, we have graphed relative ozone concentration (PPM) between days 100 and 246 at altitudes 16, 20, 26, and 31 km [6]. Results are shown in fig. 4.

The graphs for 16 and 20 km show distinctly anti-correlated behavior. While one is rising, the other is falling. The exception between days 234 and 246 occurs at the start of ozone hole formation. This behavior has a simple dynamical explanation. The ozone layer rises and falls over time. The peak concentration in ozone lies between 16 and 20 km. When the layer rises, air richer in ozone appears at 20 km and air poorer in ozone appears at 16 km. When the layer falls, the opposite occurs. This anti-correlation is
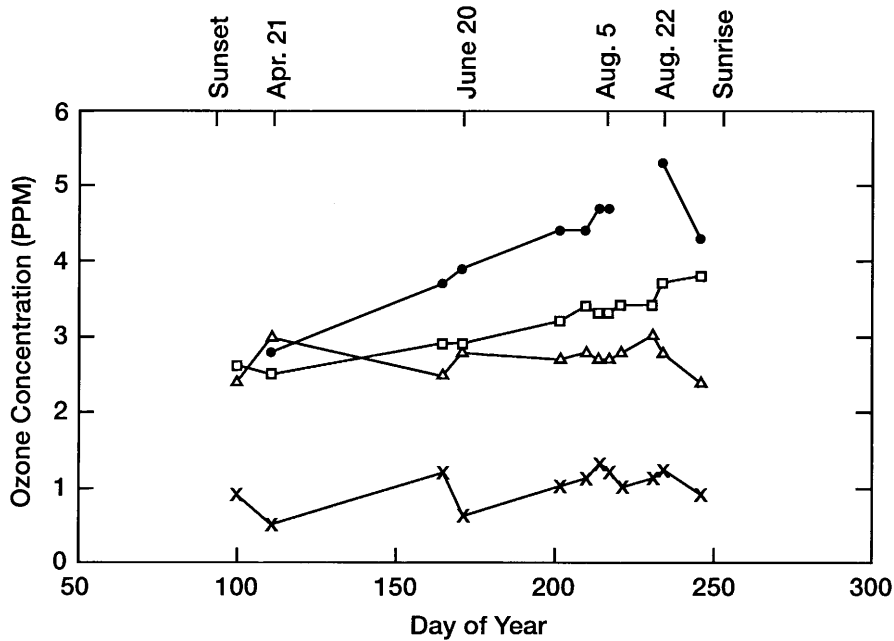
Fig. 4. – Relative ozone concentration *vs.* day of year at four altitudes over South Pole, 1986 ($\times$ 16 km, $\triangle$ 20 km, $\square$ 26 km, $\bullet$ 31 km).

simply a manifestation of fluctuations in the altitude of the ozone layer.

To extend this analysis, we have computed average ozone concentrations for time periods P_1 (days 100 to 171) and P_2 (days 202 to 234). According to this fluctuation theory, the 41% increase from P_1 to P_2 at 16 km should be compensated by a decrease at 20 km. Instead, fig. 4 shows a 4% increase. Further, this increase at 20 km is apparently correlated with a 24% increase at 26 km and a 35% increase at 31 km.

To attempt to explain these increases, we first note two remarkable aspects of the graphs for 26 and 31 km shown in fig. 4:

i) Both graphs show essentially constant slopes: 0.0082 PPM/day at 26 km (days 100 to 246), and 0.0179 PPM/day at 31 km (days 111 to 217).

ii) When these rates are expressed in absolute terms, they have essentially the same value: 6.2×10^4 molecules/cm^3/s at 26 km and 6.5×10^4 molecules/cm^3/s at 31 km.

That is, the concentration of ozone increases at an essentially constant rate at both 26 and 31 km over South Pole through most of the winter. This increase is not discernible at 16 and 20 km.

Two mechanisms are generally responsible for the increase in the concentration of ozone: production and transport.

Production: Direct sunlight is the principal form of energy driving the production of atmospheric ozone. In the absence of sunlight, the most energetic alternate is radiation associated with "auroral absorption" and "polar cap absorption" [2]. Auroral absorption refers to high-frequency radio absorption in the auroral zone and occurs during auroras

and magnetic disturbances. Polar cap absorption refers to super high-frequency radio absorption throughout the polar region and occurs during strong solar flares.

To estimate an upper limit on the contribution of auroral absorption events to the increase in the concentration of ozone at 26 and 31 km, we have assumed extreme values for the number flux and energy of photons associated with these events [7]: 10^5 /cm^2/s and 100 keV. The optical depth of X-rays with this energy is about 34 km [8]. Assuming all radiant energy is converted to ionization of oxygen molecules in a 20 km interval centered at 34 km, then the ionization rate in this interval is 4.13×10^3 ions/cm^3/s, where the ionization potential for O_2 is 12.1 eV. Electrons liberated by ionization generally attach to O_2 molecules. (N_2 molecules do not form stable negative ions.) The O_2 electron affinity is only 0.46 eV, so electrons are repeatedly dissociated in collisions between negative O_2 ions and O_2 and N_2 molecules. These electrons eventually react with positive O_2 ions [8] according to

(13)
$$O_2^+ + e \longrightarrow O(^1D) + O(^3P) + 5\,eV.$$
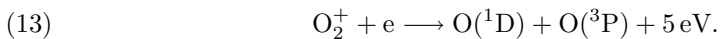
These oxygen atoms then recombine with oxygen molecules to form ozone. The rate of ozone production is twice the rate of ion production, or $\sim 8 \times 10^3$ molecules/cm^3/s.

Similarly, ionization rates associated with polar cap absorption events are ~ 75 ions/cm^3/s at 26 km and ~ 100 ions/cm^3/s at 31 km [2]. We estimate that the rates of ozone production are twice these ionization rates: ~ 150 molecules/cm^3/s at 26 km and ~ 200 molecules/cm^3/s at 31 km.

To summarize, the rate of increase for the concentration of ozone at 26 and 31 km inferred from fig. 4 is 6.5×10^5 molecules/cm^3/s. The rates corresponding to auroral absorption and polar cap absorption events are less than $\sim 8 \times 10^3$ and $\sim 2 \times 10^2$ molecules/cm^3/s. Further, these events are intermittent, so the average rates over several months are possibly orders of magnitude less. Clearly, neither kind of event can produce the increases indicated in fig. 4.

Transport: A simple diffusion model can account for the constant rates of increase shown in fig. 4. As a first-order approximation, consider a flat-earth model in which the concentration of ozone at fixed altitude z and time t_0 is given by $C(t_0; x, y) = A + B(x^2 + y^2)$ where $r \equiv (x^2 + y^2)^{1/2}$ denotes distance from South Pole. Further, assume that the concentration of ozone $C(t; x, y)$ evolves by eddy diffusion for $t > t_0$. The fundamental solution of the diffusion equation in two space dimensions is given by

$$K(t; x, y) = \frac{1}{4\pi D t} \exp\left[-\frac{x^2 + y^2}{4Dt} \right],$$

where D denotes the coefficient of eddy diffusion. Then the concentration of ozone at time t ($> t_0$) is given by the convolution of the fundamental solution with the initial concentration:

$$C(t; x, y) = \int_{-\infty}^{\infty} du \int_{-\infty}^{\infty} dv \cdot C(t_0; x, y) \cdot K(t - t_0; x - u, y - v)$$

$$= A + B(x^2 + y^2) + 4BD(t - t_0).$$

This model succeeds in predicting the constant rates of increase (4BD) in ozone concentration at 26 and 31 km. The overall relative constancy at lower altitudes may be attributed to the suppression of longer-range eddy diffusion by the circumpolar vortex.

Despite the success of this theory in accounting for the constant slopes at 26 and 31 km shown in fig. 4, it does not account for the difference between these slopes. Horizontal eddy diffusion on this scale implies discernable vertical eddy diffusion. Mixing between 26 and 31 km would tend to produce equal slopes expressed in terms of PPM/day. The measured results indicate a complete lack of mixing, however. Gross transport is even less likely to provide a satisfactory explanation for the regularity in these graphs.

Radio-emissions: A third mechanism with the potential to explain the principal features of the graphs at 26 and 31 km is radio-emission by a uniformly distributed population of sub-micron radioactive particles. As sunset approaches, the air cools. The polar vortex forms and the encircled air stabilizes. Ice crystals nucleated at 16 and 20 km scavenge these particles and eliminate them by gravitational settling. Particles at 26 and 31 km settle slowly and do not appear at 20 km before day 202.

Such particles would provide an essentially constant source of radio emissions above 20 km between days 100 and 246. Isotopes of plutonium decay primarily by emission of α-particles with energy ~ 5 MeV [9]. If this energy were converted entirely to ionization of O_2, then each emission would produce $\sim 4 \times 10^5$ ions and so, according to eq. (13), $\sim 8 \times 10^5$ ozone molecules. Given the production rate indicated in fig. 4, the corresponding α-particle emission rate would be $\sim 8 \times 10^{-2}$ /cm^3/s. However, no source for such particles has been found. (A massive release of radioactive particles began at Chernobyl on April 26, 1986 (day 116). Any influence of this release on the production of ozone over South Pole between days 111 and 234 either by transport of particles to South Pole or transport of α-emissions along the Earth's magnetic field lines would be surprising.)

This analysis has failed to account for the increase in ozone during winter at the level of the ozone layer. Unfortunately, the variability in the data hampers further analysis. For example, figs. 1 and 5 show increases of 52% and 51% between days 111 and 217 in the 19 and 14 km intervals. In contrast, fig. 4 shows increases of -10% and 140% in this same time period at 20 and 16 km.

2`8. *Water*. – Figure 3 shows a systematic decrease in temperature at three altitudes above South Pole about the time of sunset. Temperature continues to decrease throughout winter to the values shown in fig. 6. As temperature decreases, relative humidity increases. The object of this section is to quantify this relation.

The Clausius-Clapeyron equation takes the following form for equilibrium water vapor density over an ice surface [10]:

$$\rho_e(T) = \rho_e(T_0)\frac{T_0}{T}\exp\left[\frac{ML_i}{R}\cdot\left(\frac{1}{T_0}-\frac{1}{T}\right)\right],$$

where

ρ_e is the equilibrium water vapor density over an ice surface (gm/cm^3),

T is the ambient air temperature (K),

T_0 is the reference air temperature (273 K),

$\rho_e(T_0) = 4.98 \times 10^{-6}$ gm/cm^3,

M is the molecular weight of water (18 gm/mole),

L_i is the latent heat of sublimation for ice (2825 J/gm),

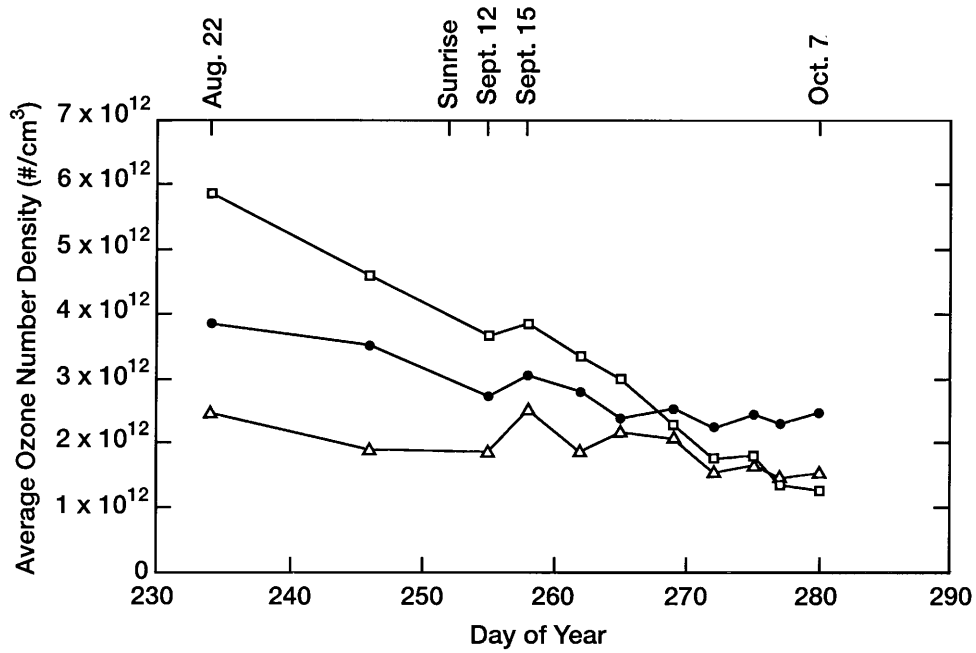Fig. 5. – Average ozone number density *vs.* day of year near sunrise (∼ September 9) for three 5 km altitude intervals over South Pole, 1986 (△ 14 km, □ 19 km, ● 24 km).
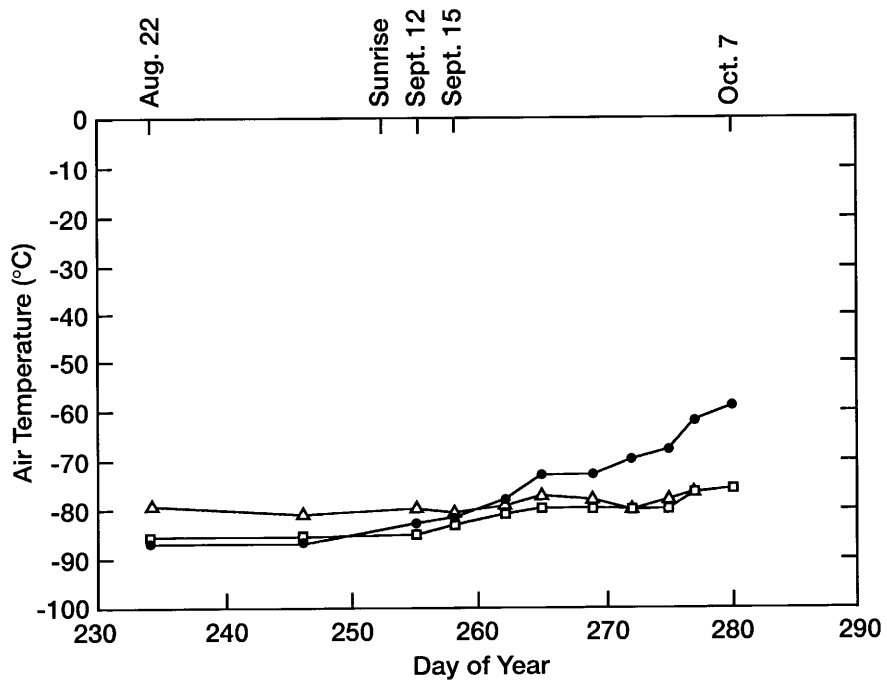
Fig. 6. – Air temperature *vs.* day of year near sunrise (∼ September 9) at three altitudes over South Pole, 1986 (△ 14 km, □ 19 km, ● 24 km).

R is the gas constant ($8.3144\,\mathrm{J/K/mole}$).

The data used in this analysis [6] have been reported in terms of a standard atmosphere, where altitude has a deterministic functional dependence on atmospheric pressure. Then for constant altitude and fixed water vapor density relative to the density of air, the partial pressure of water vapor is also constant. In this case, water vapor density ($\mathrm{gm/cm^3}$) is inversely proportional to temperature: $\rho(T) \propto 1/T$. Let RH denote relative humidity and T_1 (K) denote a given reference temperature at which RH is specified. Then

$$(14) \qquad RH(T) \equiv \frac{\rho(T)}{\rho_{\mathrm{e}}(T)}$$

$$\approx \frac{RH(T_1)\rho_{\mathrm{e}}(T_0)(T_0/T)\exp\left[(ML_{\mathrm{i}}/R)(1/T_0 - 1/T_1)\right]}{\rho_{\mathrm{e}}(T_0)(T_0/T)\exp\left[(ML_{\mathrm{i}}/R)(1/T_0 - 1/T)\right]}$$

$$= RH(T_1)\exp\left[\frac{ML_{\mathrm{i}}}{R}\left(\frac{1}{T} - \frac{1}{T_1}\right)\right].$$

Using ambient air temperatures shown in figs. 3 and 6, and assuming $RH = 0.1$ on day 57, we have used this expression to project values of RH on day 234. The results are 679.8 at 24 km, 453.2 at 19 km, and 123.9 at 14 km.

Of course, these extraordinary values are never actually attained. Relative humidity over 1.02 is rarely observed in nature. Instead, as the temperature falls at any given altitude, the relative humidity increases until particles in the air are activated as ice-forming nuclei. Ice crystals growing on these particles fall through regions with varying values of temperature and water vapor density. In an environment of super-saturation, ice crystals capture water vapor, and in an environment of sub-saturation, they release it. On balance, ice drives water vapor density in a region toward its saturation value.

This process also tends to eliminate particles from the ozone layer. Particles that are most active as ice-forming nuclei depart the ozone layer first. As the temperature continues to fall, the most active of the remaining particles take their turn. They nucleate, convert water vapor in excess of saturation to ice, and settle out of the layer. These considerations set the expectation that by day 234 air in the ozone layer has very low particle count and water vapor density near saturation.

3. – Ozone hole formation

This section advances an alternative to the catalytic chlorine/bromine theories of ozone hole formation. It proposes instead that the ozone hole is formed by the catalytic action of extraterrestrial particles.

In broad outline, a massive influx of extraterrestrial particles first arrives at the ozone layer several weeks before sunrise. The water these particles adsorb during settling forms a tightly bound monolayer. Water and ozone that subsequently adsorb on this monolayer form an uncondensed phase resembling a 2-dimensional gas. A variety of reactions are possible. O_3 may react with itself, or it may react with H_2O to produce H_2O_2. O_3 may react with H_2O_2, or H_2O_2 may react with itself to recover H_2O. Each reaction yields O_2, which represents a corresponding net loss in O_3.

Prior to sunrise, some fraction of H_2O_2 may desorb from particle surfaces into the atmosphere. H_2O_2 accumulates until sunrise, when it is subject to rapid photo-dissociation.

TABLE V. – *Percentage change in ozone number density* [O_3] *for three altitude intervals and four time periods.*

	P_1	P_2	P_3	Total
24 km	-29%	12%	-26%	-41%
19 km	-37%	5%	-54%	-69%
14 km	-23%	34%	-38%	-36%

The liberated O combines with O_2 to restore O_3 according to reaction (2). Despite the recovery of ozone by this mechanism, sunlight also alters reaction rates at particle surfaces and on balance hastens the formation of the ozone hole.

The details of this theory are developed in subsects. **3**˙1 through **3**˙7. In particular, subsect. **3**˙1 highlights features in field measurements that a viable theory of ozone hole formation should explain. Subsection **3**˙2 examines the evolving distribution of extraterrestrial particles as they settle through the ozone layer. Subsection **3**˙3 applies diffusion theory to field measurements to estimate capture efficiency—the probability that a collision between an ozone molecule and a particle results in the destruction of the molecule. Subsection **3**˙4 details the role of water in this theory. Subsection **3**˙5 proposes a specific system of chemical reactions at particle surfaces as the basis for the formation of the ozone hole. Subsection **3**˙6 derives a quantitative theory of ozone depletion that unifies the concepts advanced in subsects. **3**˙2 through **3**˙5. Subsection **3**˙7 shows how this unified theory accounts for the major features in ozone hole formation indicated in subsect. **3**˙1. Finally, subsect. **3**˙7 provides a summary and conclusions.

3˙1. *Field measurements.* – According to fig. 2, the ozone hole starts to form on day 234, about 18 days before first direct sunlight at sunrise (Appendix A). The total mass of ozone decreases at a constant rate between days 234 and 255. It then increases abruptly between days 255 and 258, three to six days after first exposure to direct sunlight. The decrease resumes at a steeper rate between days 258 and 272, and continues at a more moderate rate between days 272 and 280.

Graphs in fig. 5 show average ozone number density for the 5 km altitude intervals centered at 14, 19, and 24 km. The majority of the ozone in the ozone layer is contained in the 19 km interval. All three graphs reproduce the trends shown in fig. 2: a decrease in time period P_1 (days 234 to 255), an increase in time period P_2 (days 255 to 258), and a decrease in time period P_3 (days 258 to 272). Note that the three time periods occur essentially before, during, and after sunrise. (According to Appendix A, the fraction of the solar disk visible at 19 km increases during P_2 from 32% to 77%.)

Percentage changes in average ozone number density are given in table V. The column labeled "Total" gives the net percentage change over the total time period (from the beginning of P_1 to the end of P_3). The largest decreases in P_1 and P_3 and the smallest increase in P_2 occur at 19 km. The total decreases at 14 and 24 km are comparable, and are less than 60% of the total decrease at 19 km. Ozone number densities at 24 and 14 km appear to have reached their minima by days 265 and 272 (fig. 5). The number density at 19 km decreases up to day 280 at least.

Note that P_1 and P_3 have different durations. To rationalize these differences, we have also expressed ozone depletion during P_1 and P_3 in terms of a fractional depletion

TABLE VI. – *Average fractional depletion rates (day^{-1}) for [O_3] for three altitude intervals and two time periods.*

	$FDR(P_1)$	$FDR\ (P_3)$
24 km	0.016	0.021
19 km	0.022	0.055
14 km	0.013	0.034

rate *FDR* defined as a time average of the logarithmic time derivative of [O_3]:

$$FDR(P) \equiv \frac{-1}{t_2 - t_1} \int_{t_1}^{t_2} \left(\frac{1}{[O_3](t)} \frac{d[O_3](t)}{dt} \right) dt = \frac{\ln\left([O_3](t_1)/[O_3](t_2) \right)}{t_2 - t_1},$$

where P denotes the time period (t_1, t_2). Values of *FDR* computed from data given in fig. 5 appear in table VI Note that *FDR* at 14 and 19 km are about 2.5× larger in P_3 than in P_1; *FDR* at 24 km is only about 1.3× larger.

Two other functions will also play a role in assessing the viability of this theory. The first is *RD* (Relative Density), the ozone number density at the end of P_1 relative to the density at the beginning of P_1: $RD \equiv [O_3](T)/[O_3](0)$. Table VII shows that *RD* is a decreasing function of [O_3](0), *i.e.*, the larger the value of [O_3] at the beginning of P_1, the smaller the relative value of [O_3] at the end of P_1. If [O_3] were a simple exponential function of time, *RD* would be independent of [O_3](0).

The second function is *RB* (Relative "Bump"), the change in ozone number density during P_2 divided by the change during P_1: $RB \equiv \Delta[O_3](P_2)/\Delta[O_3](P_1)$. *RB* is simply a measure of the relative magnitude of the "bump" in ozone number density at sunrise. Table VII shows that *RB* is also a decreasing function of [O_3](0): the larger the value of [O_3] at the beginning of P_1, the smaller the change in [O_3] during P_2 relative to the change in [O_3] during P_1.

3˙2. *Extraterrestrial particle influx*. – Subsection **2**˙8 sets the expectation that by mid winter air in the ozone layer over South Pole would have very low ambient particle count. Part I of this paper predicts the invasion of this environment by extraterrestrial particles at the start of ozone hole formation and estimates that the concentration of these particles lies between 500 and 2000 m^{-3} throughout the period of ozone hole formation. The object of this section is to analyze the evolution of the size distribution of these particles during this period.

TABLE VII. – *Ozone number density at the beginning of $P_1([O_3](0))$, relative ozone number density at the end of $P_1(RD \equiv [O_3](T)/[O_3](0))$, and the change in ozone number density during P_2 divided by the change during $P_1(RB \equiv \Delta[O_3](P_2)/\Delta[O_3](P_1))$ for three altitude intervals.*

Altitude (km)	$[O_3](0)\ (\#/cm^3)$	RD (fraction)	RB (fraction)
14	2.47×10^{12}	0.77	1.10
24	3.85×10^{12}	0.71	0.30
19	5.86×10^{12}	0.63	0.09

TABLE VIII. – *Time (days) for a (spherical) particle to settle from the top of the atmosphere to a given altitude for three particle radii and three altitudes.*

	$r = 2.5\,\mu\mathrm{m}$	$r = 5.0\,\mu\mathrm{m}$	$r = 7.5\,\mu\mathrm{m}$
$24\,\mathrm{km}$	23.1	9.0	5.0
$19\,\mathrm{km}$	36.0	12.7	6.7
$14\,\mathrm{km}$	51.0	16.7	8.5

The terminal velocity for a (spherical) particle falling in air is given by an empirical extension of Stokes' Formula [11]:

$$v = \frac{2\rho\tilde{g}r^2}{9\mu}\left(1 + A\frac{\lambda}{r} + Q\frac{\lambda}{r}e^{-br/\lambda}\right),$$

where

v is the particle terminal velocity (cm/s),

ρ is the effective particle density (gm/cm^3),

$\tilde{g}$ is the gravitational acceleration ($\sim 980\,\mathrm{cm/s^2}$),

r is the effective particle radius (cm),

μ is the dynamic viscosity of air (gm/cm/s, [4]),

λ is the mean free path of air molecules (cm, [4]),

$A = 0.77$,

$Q = 0.40$,

$b = 1.62$.

Assigning densities to particles is problematical. To illustrate, F. Prodi discovered cavities in magnetic spherules in 1968. We take $\rho = 3.5\,\mathrm{gm/cm^3}$ as the representative value in subsequent calculations [1]. A, Q, and b are experimentally determined dimensionless constants. The values given here are for glass spheres settling in air.

We have integrated this function to determine the time for particles of three given radii to settle from the top of the atmosphere to three given altitudes. Results are given in table VIII:

  i) An extraterrestrial particle stream that produces particles of these sizes contributes to the 19 km interval starting ~ 7 days after the Earth enters the stream and ending ~ 36 days after the Earth exits the stream;

 ii) a shower lasting 20 days contributes particles for ~ 38 days at 24 km, ~ 49 days at 19 km, and ~ 63 days at 14 km;

iii) larger particles appear first but smaller particles reside longer in a given altitude interval;

TABLE IX. – *Particle number densities (#/cm^3) for three radii and three altitudes. Each value corresponds to a constant particle number flux of* $1.56 \times 10^{-3}/\text{cm}^2/\text{s}$.

	$r = 2.5\,\mu\text{m}$	$r = 5.0\,\mu\text{m}$	$r = 7.5\,\mu\text{m}$
24 km	25.5×10^{-4}	8.4×10^{-4}	4.1×10^{-4}
19 km	34.9×10^{-4}	10.0×10^{-4}	4.7×10^{-4}
14 km	40.7×10^{-4}	10.9×10^{-4}	4.9×10^{-4}

iv) the influx of particles at 24 km begins ~ 4 days before the influx at 14 km.

Finally, note that for particles of a given size settling in a quiescent atmosphere, particle number flux is the product of number density and terminal velocity. We have used this relation to estimate the variation in number density as a function of particle radius and altitude for a fixed value of particle number flux. (A flux of 1.56×10^{-3} particles/cm^2/s corresponds to a number density of 10^{-3} particles/cm^3 for $5.0\,\mu$m radius particles at 19 km.) Results are given in table IX.

3˙3. *Diffusion of ozone*. – According to subsect. **2**˙6, without some special external influence, ozone number density should remain constant over South Pole in all three altitude intervals from the beginning of P_1 to the end of P_3. To explain the decline in ozone number density shown in figs. 2 and 5, we have hypothesized that the ozone hole is formed by the destruction of ozone at extraterrestrial particle surfaces. The next step in analyzing this possibility is to examine the relation between ozone number density and particle number density.

Diffusion theory (Appendix B) provides the relation

$$\frac{\mathrm{d}[\mathrm{O}_3]}{\mathrm{d}t} = -4\pi\varepsilon D^* RN[\mathrm{O}_3],$$

where

[O$_3$] is the ozone number density (#/cm^3),

ε is the capture efficiency (fraction),

D^* is the diffusion coefficient for O$_3$ in air (cm^2/s),

R is the particle radius (cm),

N is the particle number density (#/cm^3).

Capture efficiency is the probability that a collision between an ozone molecule and a particle results in the destruction of the molecule. (The reciprocal of ε is just the expected number of collisions between ozone molecules and particles per capture.)

The solution of this equation is given by

$$[\mathrm{O}_3](t) = [\mathrm{O}_3](t_0) \cdot \exp\left[-4\pi\varepsilon D^* RN \cdot (t - t_0)\right],$$
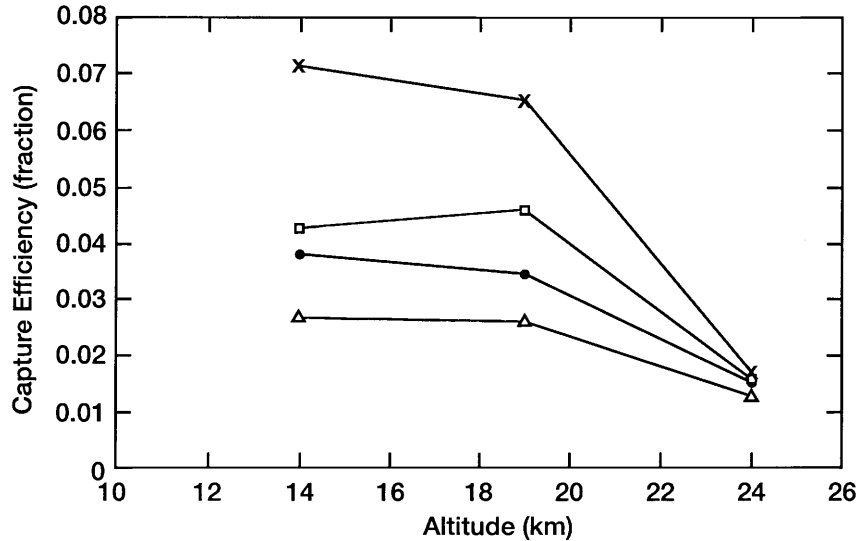
Fig. 7. – Estimates of capture efficiency *vs.* altitude for two time periods and two models for the influx of extraterrestrial particles at the ozone layer ($\times$ post-sunrise, uniform arrival; $\square$ post-sunrise, non-uniform arrival; $\bullet$ pre-sunrise, non-uniform arrival; $\triangle$ pre-sunrise, uniform arrival).

where t_0 denotes a reference time and $[O_3](t_0)$ denotes ozone number density at t_0. After rearrangement,

$$\varepsilon = \frac{-\ln\left([O_3](t)/[O_3]\left(t_0\right)\right)}{4\pi D^* R N\left(t - t_0\right)}.$$

To gauge the applicability of diffusion theory, we have evaluated this expression using two models for the influx of extraterrestrial particles at the ozone layer (19 km). In the first, we have assumed that the particle number flux is 1.56×10^{-3} particles/cm^2/s and the average particle radius is $5.0\,\mu$m throughout P_1 and P_3. In the second, we have assumed the same value for the flux but that the particle distribution evolves such that the average radius is $7.5\,\mu$m during P_1 and $2.5\,\mu$m during P_3. The first model represents a uniform influx during ozone hole formation produced by the arrival of particles at the top of the atmosphere over a sustained period; the second represents a non-uniform influx produced by the arrival of particles over a relatively short period (subsect. **3**˙2). We have taken values for $[O_3]$ from fig. 5, corresponding values for N from table IX, and values for D^* computed according to Appendix B. Estimates of capture efficiency are given in fig. 7:

i) capture efficiency is uniformly small for the 24 km interval (~ 0.015),

ii) capture efficiency tends to increase with decreasing altitude both pre- and post-sunrise,

iii) post-sunrise estimates are larger than the corresponding pre-sunrise estimates in all three altitude intervals,

iv) estimates for the uniform arrival model bracket the estimates for the non-uniform arrival model.

3˙4. *The role of water*. – The object of this section is to assess the role of water in the destruction of ozone at particle surfaces.

Because of intense heating, extraterrestrial particles are completely dehydrated during atmospheric entry. Water adsorbs on these particles as they settle from the top of the atmosphere through the ozone layer. We hypothesize two modes of adsorption: chemical and physical.

Extraterrestrial particles consist primarily of iron oxides and aluminum silicates [1]. In the first adsorption mode, water incorporates chemically at a particle's surface in hydrate and hydroxide complexes. The nature and degree of hydration depends on chemical and physical details of the surface, its history of exposure to water vapor, temperature, solar radiation, and other chemical constituents in the atmosphere. A particle may be incompletely hydrated when it reaches the ozone layer because of generally low water vapor density above 24 km [4]. Since smaller particles settle more slowly, they tend to be more completely hydrated at any given altitude. Hydrogen atoms in the adsorbate are generally oriented outward [12]. We adopt a conceptual model of this adsorption mode in which an extraterrestrial particle acquires a tightly bound aqueous monolayer through chemisorption [5]. Molecular orientation of the adsorbate induces a double layer electrostatic potential at the surface [13]. Θ, the effective fraction of a particle's surface covered by this monolayer, is a decreasing function of both particle radius and altitude.

The second mode is physical adsorption on this primary monolayer. The dynamics of this process are suggested by the BET adsorption model [14]. Rearrangement of the BET isotherm yields

$$(15) \qquad \theta = \frac{c \cdot RH}{(1 - RH)\big(1 + (c-1)RH\big)},$$

where

θ is the adsorbent coverage (ratio of adsorbate volume to monolayer volume),

RH is the relative humidity,

c is a parameter characterizing intermolecular affinity.

For low values of RH, θ is proportional to RH; as RH approaches unity, θ increases without limit and bulk condensation occurs. Molecules adsorbed in this mode are loosely bound to the particle. The value of θ is determined by a dynamic equilibrium between adsorption and desorption.

Although the BET model is suggestive, it is not definitive. Equation (15) generally overestimates θ for adsorption processes (including water) characterized by small values of c. A more detailed model represents molecules adsorbed on the primary monolayer as a 2-dimensional, 2-phase thermodynamic system [15, 16]. At low values of θ, molecules have high surface mobility and behave like a 2-dimensional gas. As θ increases, the 2-dimensional analog of condensation occurs. This condensed phase constitutes a secondary monolayer. High values of θ correspond to coverage by multiple monolayers.

The adsorption model developed in this section provides a basis for analyzing the trends in ozone capture efficiency shown in fig. 7. According to eq. (15), RH drives

TABLE X. – *Estimates of relative humidity (RH, fraction) pre-sunrise (P_1) and post-sunrise (P_3) at three altitudes.*

	RH (P_1)	RH (P_3)
24 km	0.89	0.18
19 km	0.97	0.41
14 km	1.00	0.89

adsorption on the primary monolayer. Assuming values of air temperature shown in fig. 6 and $RH \equiv 1.00$ in each altitude interval on day 234 (subsect. **2**·8), we have used eq. (14) to estimate RH on subsequent days in P_1 and P_3. Average values of RH for P_1 and P_3 in the three altitude intervals are given in table X. RH is apparently much higher before than after sunrise. Estimates increase with decreasing altitude in both P_1 and P_3. Note that values shown for P_1 depend on small increments in temperature, which are prone to uncertainty.

The first model represents the influx of particles of constant average size throughout the period of ozone hole formation (subsect. **3**·3). We hypothesize that capture efficiencies are relatively small at 24 km because of incomplete coverage by the primary monolayer, and are practically constant between 14 and 19 km because coverage has approached its maximum values. We attribute the larger post-sunrise capture efficiencies in this scenario to the effect of direct sunlight, which accelerates the rates of chemical reactions responsible for ozone destruction at particle surfaces.

The second model represents the influx of particles of evolving average size. Larger particles settle faster and occupy the ozone layer during P_1; smaller particles settle more slowly and occupy the ozone layer during P_3. Note that the difference in times for 7.5 and 2.5 μm radius particles to settle to 19 km ($\sim$ 29 days) is well reconciled with the time between the start of P_1 and the end of P_3 ($\sim$ 38 days). We hypothesize that coverage by the primary monolayer is more advanced for smaller particles at any given altitude because of their longer settling times. Thus, the larger values of capture efficiency after sunrise. The low value of RH after sunrise at 24 km may negate this effect and bring the pre- and post-sunrise values of capture efficiency to essential equality.
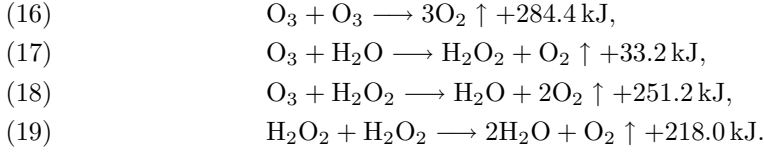
These two scenarios represent opposite extremes. The actual influx is undoubtedly an interpolation. The corresponding capture efficiencies are undoubtedly also interpolations. At one extreme, the difference between pre- and post-sunrise values of capture efficiency is attributable to photosensitivity of reaction rate coefficients for reactions responsible for ozone destruction at particle surfaces. At the other extreme, the difference is attributable to the degree of particle surface coverage by the primary monolayer. The actual physical situation may lie somewhere in between.

3·5. *Surface chemistry*. – The object of this section is to outline a chemical process that accounts for ozone hole formation by the destruction of ozone at extraterrestrial particle surfaces. To make this account tractable, we assume

  i) chemical reactions occur on the primary adsorption monolayer described in subsect. **3**·4,

 ii) coverage of the primary monolayer is relatively low [15],

iii) reactants diffuse freely on the primary monolayer [16].

For the present, we ignore condensed phases, variable surface potentials, and chemical catalytic effects of the adsorbent. In fact, to estimate reaction rates, we have assumed that reactants behave in effect like an ideal gas. A more complete system model combining surface chemistry, adsorption/desorption, and atmospheric diffusion is derived in subsect. **3**˙6. Details of the actual surface chemistry are undoubtedly very much more complex than the account given in this paper.

We propose that the following system of reactions at extraterrestrial particle surfaces is responsible for ozone hole formation:

$$(16) \qquad \qquad O_3 + O_3 \longrightarrow 3O_2 \uparrow +284.4 \, \text{kJ},$$

$$(17) \qquad \qquad O_3 + H_2O \longrightarrow H_2O_2 + O_2 \uparrow +33.2 \, \text{kJ},$$

$$(18) \qquad \qquad O_3 + H_2O_2 \longrightarrow H_2O + 2O_2 \uparrow +251.2 \, \text{kJ},$$

$$(19) \qquad \qquad H_2O_2 + H_2O_2 \longrightarrow 2H_2O + O_2 \uparrow +218.0 \, \text{kJ}.$$

Water and ozone are both polar [12], which suggests that residence times at particle surfaces are significant. Residence times for hydrogen peroxide are less certain. Molecular oxygen clearly escapes into the atmosphere as soon as it is produced.

Each equation includes the enthalpy evolved in the reaction. Each enthalpy is positive, *i.e.*, each reaction is exothermic. Standard enthalpies (gas phase) used in the calculations: $\Delta H_f^0(O_2) = 0.0 \, \text{kJ/mol}$, $\Delta H_f^0(O_3) = 142.2 \, \text{kJ/mol}$, $\Delta H_f^0(H_2O) = -241.8 \, \text{kJ/mol}$, $\Delta H_f^0(H_2O_2) = -132.8 \, \text{kJ/mol}$. Adjustments for lower temperatures and pressures yield essentially the same results.

Finally, the rate equations for $[O_3]_s$, $[H_2O]_s$ and $[H_2O_2]_s$ corresponding to system (16) through (19) are given by

$$(20) \qquad \frac{d[O_3]_s}{dt} = Q_{O_3}\left([O_3]_s, [H_2O]_s, [H_2O_2]_s\right)$$
$$\equiv -2\beta_1 [O_3]_s^2 - \beta_2 [H_2O]_s [O_3]_s - \beta_3 [H_2O_2]_s [O_3]_s,$$

$$(21) \qquad \frac{d[H_2O]_s}{dt} = Q_{H_2O}\left([O_3]_s, [H_2O_2]_s, [H_2O_2]_s\right)$$
$$\equiv -\beta_2 [O_3]_s [H_2O]_s + \beta_3 [O_3]_s [H_2O_2]_s + 2\beta_4 [H_2O_2]_s^2,$$

$$(22) \qquad \frac{d[H_2O_2]_s}{dt} = Q_{H_2O_2}\left([O_3]_s, [H_2O]_s, [H_2O_2]_s\right)$$
$$\equiv \beta_2 [O_3]_s [H_2O]_s - \beta_3 [O_3]_s [H_2O_2]_s - \beta_4 [H_2O_2]_s^2,$$

where the subscript "s" denotes surface density. The rate coefficients β_1 through β_4 for these surface reactions may depend on a variety of variables including temperature and solar radiation.

3˙6. *Unified model of ozone depletion.* – The object of this section is to consolidate the results of subsects. **3**˙2 through **3**˙5 in a quantitative model for ozone depletion. In particular, it develops a system of equations relating the evolution of particle distributions, atmospheric diffusion, adsorption, and surface chemistry. This model will be used in subsect. **3**˙7 to provide an analysis of the major features of ozone hole formation indicated in subsect. **3**˙1.

3˙6.1.   Diffusion. Diffusion theory (Appendix B) provides the following estimate for the concentration ($\#/\text{cm}^3$) of species X a distance r from the center of a particle of radius R:

$$C_X(r) = C_X(R)\frac{R}{r} + C_X(\infty)\left(1 - \frac{R}{r}\right),$$

where $r > R$, and X may represent O_3, H_2O, or H_2O_2. The net transport by diffusion ($\#/\text{s}$) of species X from the particle's surface is given by

$$(23) \qquad -4\pi R^2 D_X^* \frac{\partial C_X}{\partial r}\bigg|_{r=R} = 4\pi R D_X^* \big(C_X(R) - C_X(\infty)\big).$$

3˙6.2.   Production. The normalized rate of chemical production ($\#/\text{cm}^2/\text{s}$) is given by Q_X in eqs. (20), (21), and (22). The net rate of chemical production for a particle of radius R at altitude z is given by

$$(24) \qquad\qquad 4\pi R^2 \Theta(R,z) Q_X.$$

The arguments of Q_X may be written in terms of fractional coverage by substituting $[Y] = \Gamma_Y \theta_Y$, where Γ_Y denotes maximum density in monolayer coverage for species Y ($\#/\text{cm}^2$) and θ_Y denotes the fraction of the primary monolayer covered by species Y.

3˙6.3.   Adsorption. The normalized collision rate for species X at a particle's surface ($\#/\text{cm}^2/\text{s}$) is given by $C_X(R)w_X/4$ (Appendix B). The corresponding adsorption rate ($\#/\text{s}$) is given by

$$(25) \qquad\qquad 4\pi R^2 \Theta \theta_\phi \varepsilon_X C_X(R)\frac{w_X}{4},$$

where

  θ_ϕ is the fraction of the primary monolayer not covered by any of the adsorbed species,

  ε_X is the adsorption efficiency (the probability that a collision will result in an attachment to the primary monolayer).

3˙6.4.   Desorption. The rate of desorption of species X from a particle's surface ($\#/\text{s}$) is proportional to the number of molecules adsorbed on the surface:

$$(26) \qquad\qquad 4\pi R^2 \Theta \theta_X \Gamma_X \sigma_X.$$

Two conservation statements lead to two equations for variables $C_X(R)$ and θ_X. The first asserts that given conditions of quasi-equilibrium, the net rate of production of species X at a particle's surface equals the net rate of transport of X by diffusion from the surface, *i.e.*, expression (23) equals expression (24):

$$(27) \qquad\qquad R\Theta(R,z)Q_X = D_X^* \big(C_X(R) - C_X(\infty)\big).$$

Similarly, the second asserts that the desorption rate equals the net production rate plus the adsorption rate, *i.e.*, expression (26) equals the sum of expressions (24) and (25):

$$(28) \qquad 4\sigma_X \Gamma_X \theta_X = 4Q_X + \varepsilon_X w_X C_X(R)\theta_\phi.$$

Equations (27) and (28) can be combined to eliminate $C_X(R)$. The result is an equation for θ_X. When this equation is specialized to O_3, H_2O, and H_2O_2, the result is a system of coupled equations for θ_{O_3}, θ_{H_2O}, and $\theta_{H_2O_2}$:

$$(29) \qquad \left(\varepsilon_{O_3} w_{O_3} R\Theta\theta_\phi + 4D^*_{O_3}\right)Q_{O_3} +$$
$$+ \varepsilon_{O_3} w_{O_3} D^*_{O_3} C_{O_3}(\infty)\theta_\phi - 4\sigma_{O_3} D^*_{O_3}\Gamma_{O_3}\theta_{O_3} = 0,$$

$$(30) \qquad \left(\varepsilon_{H_2O} w_{H_2O} R\Theta\theta_\phi + 4D^*_{H_2O}\right)Q_{H_2O} +$$
$$+ \varepsilon_{H_2O} w_{H_2O} D^*_{H_2O} C_{H_2O}(\infty)\theta_\phi - 4\sigma_{H_2O} D^*_{H_2O}\Gamma_{H_2O}\theta_{H_2O} = 0,$$

$$(31) \qquad \left(\varepsilon_{H_2O_2} w_{H_2O_2} R\Theta\theta_\phi + 4D^*_{H_2O_2}\right)Q_{H_2O_2} +$$
$$+ \varepsilon_{H_2O_2} w_{H_2O_2} D^*_{H_2O_2} C_{H_2O_2}(\infty)\theta_\phi - 4\sigma_{H_2O_2} D^*_{H_2O_2}\Gamma_{H_2O_2}\theta_{H_2O_2} = 0,$$

where

$$\theta_\phi \equiv 1 - \theta_{O_3} - \theta_{H_2O} - \theta_{H_2O_2},$$
$$Q_{O_3} \equiv -2\beta_1 \Gamma^2_{O_3}\theta^2_{O_3} - \beta_2 \Gamma_{O_3}\Gamma_{H_2O}\theta_{O_3}\theta_{H_2O} - \beta_3 \Gamma_{O_3}\Gamma_{H_2O_2}\theta_{O_3}\theta_{H_2O_2},$$
$$Q_{H_2O} \equiv -\beta_2 \Gamma_{O_3}\Gamma_{H_2O}\theta_{O_3}\theta_{H_2O} + \beta_3 \Gamma_{O_3}\Gamma_{H_2O_2}\theta_{O_3}\theta_{H_2O_2} + 2\beta_4 \Gamma^2_{H_2O_2}\theta^2_{H_2O_2},$$
$$Q_{H_2O_2} \equiv \beta_2 \Gamma_{O_3}\Gamma_{H_2O}\theta_{O_3}\theta_{H_2O} - \beta_3 \Gamma_{O_3}\Gamma_{H_2O_2}\theta_{O_3}\theta_{H_2O_2} - 2\beta_4 \Gamma^2_{H_2O_2}\theta^2_{H_2O_2}.$$

The algorithm for estimating ozone depletion is now immediate. Assuming $C_{O_3}(\infty)$, $C_{H_2O}(\infty)$, and $C_{H_2O_2}(\infty)$ are essentially constant on the time scale for reactions (16) through (19) to approach equilibrium, we solve system (29), (30), and (31) for θ_{O_3}, θ_{H_2O} and $\theta_{H_2O_2}$. We then use eq. (27) to estimate $C_{O_3}(\infty)$, $C_{H_2O}(\infty)$, and $C_{H_2O_2}(\infty)$. Finally, identifying $[O_3]$ with $C_{O_3}(\infty)$, $[H_2O]$ with $C_{H_2O}(\infty)$, and $[H_2O_2]$ with $C_{H_2O_2}(\infty)$, the time-dependent diffusion equation (Appendix B) provides the means to estimate ambient concentrations of O_3, H_2O, and H_2O_2 over the long term:

$$(32) \qquad \frac{d[O_3]}{dt} = 4\pi NRD^*_{O_3}\left(C_{O_3}(R) - [O_3]\right),$$

$$(33) \qquad \frac{d[H_2O]}{dt} = 4\pi NRD^*_{H_2O}\left(C_{H_2O}(R) - [H_2O]\right),$$

$$(34) \qquad \frac{d[H_2O_2]}{dt} = 4\pi NRD^*_{H_2O_2}\left(C_{H_2O_2}(R) - [H_2O_2]\right).$$

3`7. *Data analysis*. – The object of this section is to show how the extraterrestrial particle theory developed in subsects. **3**`2 through **3**`6 can account for the major features of ozone hole formation indicated in subsect. **3**`1. In particular,

1) Ozone hole formation begins three weeks before sunrise in all three altitude intervals.

Magnetic spherule data presented in Part I of this paper is strongly suggestive of high concentrations of extraterrestrial particles in the ozone layer over South Pole precisely at ozone hole formation. A theory of stratospheric ice crystal coalescence developed in Part I enabled us to project a massive influx of extraterrestrial particles at 19 km over South Pole in potentially three pulses: Aug. 21-Sept. 2, Sept. 5-Sept. 13, and Sept. 15-Oct. 13. Coincidentally, fig. 2 shows that formation of the ozone hole begins about Aug. 22 and extends beyond Oct. 7.

Figure 5 shows that ozone concentrations decline in all three altitude intervals between Aug. 22 and Sept. 12 (22 days). According to Appendix A, sunrise occurs on about Sept. 9, when direct sunlight first arrives over South Pole at 19 km. The spike in ozone concentration between Sept. 12 and Sept. 15 occurs when the fraction of the solar disk visible at 19 km increases from 32% to 77%.

According to table VIII, a $7.5\,\mu$m radius particle settles from 24 to 14 km in ~ 3.5 days. This small difference gives the appearance of simultaneous initiation of ozone hole formation in all three altitude intervals.

Finally, Part I projects that the concentration of extraterrestrial particles in the ozone layer over South Pole during ozone hole formation lies between 500 and $2000\,\mathrm{m}^{-3}$. Estimates of capture efficiency based on a concentration of $1000\,\mathrm{m}^{-3}$ (fig. 7) lie between 0.01 and 0.10. This numerical range confirms that this particle concentration can be effective in a diffusion-limited process of ozone destruction at particle surfaces.

2) Relative ozone number density at the end of P_1 ($RD \equiv [\mathrm{O}_3](T)/[\mathrm{O}_3](0)$) is a decreasing function of ozone number density at the beginning of P_1 ($= [\mathrm{O}_3](0)$).

The unified model of ozone depletion at particle surfaces (subsect. **3**˙6) accounts for this effect. A complete analysis is beyond the scope of this paper. The following computation is illustrative, however.

For simplicity, assume $\beta_2 = \beta_3 = \beta_4 = 0$, *i.e.*, the system of reactions at particle surfaces responsible for ozone hole formation is limited to reaction (16). In this case, eqs. (32), (27), and (20) yield

$$\frac{\mathrm{d}[\mathrm{O}_3]}{\mathrm{d}t} = 4\pi N R D^*_{\mathrm{O}_3}\big(\mathrm{C}_{\mathrm{O}_3}(R) - [\mathrm{O}_3]\big) = 4\pi N R^2 \Theta Q_{\mathrm{O}_3} = -2\beta_1\big(4\pi R^2 \Theta\big)\big(\Gamma_{\mathrm{O}_3}\theta_{\mathrm{O}_3}\big)^2.$$

$I_{\mathrm{O}_3}\theta_{\mathrm{O}_3}$ satisfies a restricted version of eq. (29):

$$-2\beta_1\big(\varepsilon_{\mathrm{O}_3} w_{\mathrm{O}_3} R\Theta\big(1 - \theta_{\mathrm{O}_3}\big) + 4D^*_{\mathrm{O}_3}\big)\big(\Gamma_{\mathrm{O}_3}\theta_{\mathrm{O}_3}\big)^2 +$$
$$+ \varepsilon_{\mathrm{O}_3} w_{\mathrm{O}_3} D^*_{\mathrm{O}_3}[\mathrm{O}_3]\big(1 - \theta_{\mathrm{O}_3}\big) - 4\sigma_{\mathrm{O}_3} D^*_{\mathrm{O}_3}\big(\Gamma_{\mathrm{O}_3}\theta_{\mathrm{O}_3}\big) = 0.$$

Assuming further that $\theta_{\mathrm{O}_3} \ll 1$,

$$A\,\big(\Gamma_{\mathrm{O}_3}\theta_{\mathrm{O}_3}\big)^2 + B\big(\Gamma_{\mathrm{O}_3}\theta_{\mathrm{O}_3}\big) - C \approx 0,$$

where

$$A \equiv 2\beta_1\big(\varepsilon_{\mathrm{O}_3} w_{\mathrm{O}_3} R\Theta + 4D^*_{\mathrm{O}_3}\big),$$
$$B \equiv 4\sigma_{\mathrm{O}_3} D^*_{\mathrm{O}_3},$$
$$C \equiv \varepsilon_{\mathrm{O}_3} w_{\mathrm{O}_3} D^*_{\mathrm{O}_3}[\mathrm{O}_3].$$

Then

$$\Gamma_{O_3}\theta_{O_3} \approx \frac{\left[B^2 + 4AC\right]^{1/2} - B}{2A} \approx \frac{C}{B}$$

for $[O_3] \ll 2\sigma_{O_3}D^*_{O_3}/(\beta_1\varepsilon_{O_3}w_{O_3}(\varepsilon_{O_3}w_{O_3}R\Theta + 4D^*_{O_3}))$. In this case,

$$(35) \qquad \frac{d[O_3]}{dt} \approx -2\beta_1\left(4\pi R^2\Theta\right)NC^2/B^2 = -E[O_3]^2,$$

where $E \equiv 2\beta_1(4\pi R^2\Theta)N(\varepsilon_{O_3}w_{O_3}/4\sigma_{O_3})^2$. The solution of this equation is

$$[O_3](t) = \frac{[O_3](0)}{E \cdot [O_3](0)t + 1}.$$

Thus,

$$(36) \qquad RD \equiv \frac{[O_3](T)}{[O_3](0)} = \frac{1}{E \cdot [O_3](0)T + 1},$$

which is clearly a decreasing function of $[O_3](0)$, and reproduces the trend for RD shown in table VII.

3) The concentration of ozone increases in a narrow time interval including sunrise in all three altitude intervals.

Figure 5 shows that the concentration of ozone spikes upward at all three altitude intervals between Sept. 12 and Sept. 15. According to Appendix A, the fraction of the solar disk visible at 19 km increases from 32% to 77% in this same interval. This observation finds an explanation in reaction (17). Prior to sunrise, some fraction of H_2O_2 produced at particle surfaces according to reaction (17) escapes into the atmosphere. This store of H_2O_2 is subject to rapid photo-dissociation at sunrise. Liberated O combines with O_2 to restore O_3 according to

$$(37) \qquad\qquad H_2O_2 + h\nu \longrightarrow H_2O + O,$$
$$(38) \qquad\qquad O + O_2 + M \longrightarrow O_3 + M.$$

Hence the spike at sunrise.

4) The change in ozone number density during P_2 relative to the change during P_1 ($RB \equiv \Delta[O_3](P_2)/\Delta[O_3](P_1)$) is a decreasing function of ozone number density at the beginning of $P_1(= [O_3](0))$.

The unified model (subsect. **3**˙6) also accounts for this effect. Since a complete analysis in this case is also beyond the scope of this paper, the following computation is likewise illustrative.

Assuming that the increment in ozone concentration in P_2 is produced by photo-dissociation of accumulated atmospheric H_2O_2, then $\Delta[O_3](P_2) = \Delta[H_2O_2](P_1)$. According to reactions (17), (18), and (19), this increment in $[H_2O_2]$ equals the corresponding decrement in $[H_2O]$. Thus,

$$DB \approx \frac{[H_2O](0) - [H_2O](T)}{[O_3](0) - [O_3](T)},$$

where T denotes the length of P_1. To estimate $[H_2O](t)$, assume $\beta_3 = \beta_4 = 0$, $\theta_{O_3} \ll 1$, $\theta_{H_2O} \ll 1$, and $[O_3](t) \approx [O_3](0)/(E \cdot [O_3](0)t + 1)$.

First consider the equations relating to O_3. Equations (32) and (27) yield

$$\frac{d[O_3]}{dt} = \left(4\pi R^2 \Theta\right) N Q_{O_3}.$$

Alternatively, the assumed form for $[O_3](t)$ implies

$$\frac{d[O_3]}{dt} \approx -E \cdot [O_3]^2.$$

Thus,

$$Q_{O_3} = -\frac{E}{\left(4\pi R^2 \Theta\right) N}[O_3]^2.$$

Further, eq. (29) takes the form

$$A_1 Q_{O_3} + C_1 [O_3] - D_1\left(\Gamma_{O_3}\theta_{O_3}\right) \approx 0,$$

where

$$
\begin{aligned}
A_1 &\equiv \varepsilon_{O_3} w_{O_3} R\Theta + 4D^*_{O_3}, \\
C_1 &\equiv \varepsilon_{O_3} w_{O_3} D^*_{O_3}, \\
D_1 &\equiv 4\sigma_{O_3} D^*_{O_3}.
\end{aligned}
$$

Substituting for Q_{O_3} and solving for $\Gamma_{O_3}\theta_{O_3}$, we obtain

$$\Gamma_{O_3}\theta_{O_3} \approx (C_1/D_1)\,[O_3] - (B_1/D_1)\,[O_3]^2,$$

where $B_1 \equiv 2\beta_1(\varepsilon_{O_3} w_{O_3} R\Theta + 4D^*_{O_3})(\varepsilon_{O_3} w_{O_3}/4\sigma_{O_3})^2$.

Analyzing the corresponding equations relating to H_2O similarly, we obtain

$$A_2\left(\Gamma_{O_3}\theta_{O_3}\right)\left(\Gamma_{H_2O}\theta_{H_2O}\right) - C_2[H_2O] + D_2\left(\Gamma_{H_2O}\theta_{H_2O}\right) \approx 0,$$

where

$$
\begin{aligned}
A_2 &\equiv \beta_2\left(\varepsilon_{H_2O} w_{H_2O} R\Theta + 4D^*_{H_2O}\right), \\
C_2 &\equiv \varepsilon_{H_2O} w_{H_2O} D^*_{H_2O}, \\
D_2 &\equiv 4\sigma_{H_2O} D^*_{H_2O}.
\end{aligned}
$$

Solving for $\Gamma_{H_2O}\theta_{H_2O}$, we obtain

$$\Gamma_{H_2O}\theta_{H_2O} \approx \frac{C_2}{A_2\left(\Gamma_{O_3}\theta_{O_3}\right) + D_2}[H_2O].$$

Further, eqs. (33), (27), and (21) yield

$$\frac{d[H_2O]}{dt} = -\beta_2\big(4\pi R^2\Theta\big)N\big(\Gamma_{O_3}\theta_{O_3}\big)\big(\Gamma_{H_2O}\theta_{H_2O}\big)$$

$$= -\frac{B_2(\Gamma_{O_3}\theta_{O_3})}{A_2\big(\Gamma_{O_3}\theta_{O_3}\big) + D_2}[H_2O],$$

where $B_2 \equiv \beta_2(4\pi R^2\Theta)N\varepsilon_{H_2O}w_{H_2O}D^*_{H_2O}$. By substituting for $\Gamma_{O_3}\theta_{O_3}$ and then for $[O_3](t)$, this equation takes the form

$$\frac{d\ln[H_2O]}{dt} \approx -\frac{B_2C_1[O_3] - B_1B_2[O_3]^2}{A_2C_1[O_3] - A_2B_1[O_3]^2 + D_1D_2} \approx \frac{F}{Gt+H},$$

where

$$F \equiv B_2C_1[O_3](0),$$
$$G \equiv D_1D_2E[O_3](0),$$
$$H \equiv A_2C_1[O_3](0) + D_1D_2,$$
$$[O_3] \ll \frac{2\sigma_{O_3}D^*_{O_3}}{\beta_1\varepsilon_{O_3}w_{O_3}\big(\varepsilon_{O_3}w_{O_3}R\Theta + 4D^*_{O_3}\big)}.$$

The solution of this equation is

$$[H_2O](t) = [H_2O](0)\cdot\left(1 + \frac{G}{H}t\right)^{-F/G},$$

so,

$$RB = \frac{[H_2O](0) - [H_2O](T)}{[O_3](0) - [O_3](T)} \approx \frac{[H_2O](0)}{[O_3](0)}\left(\frac{\big(1 + (G/H)T\big)^{F/G} - 1}{\big(1 + (G/H)T\big)^{F/G}}\right)\left(\frac{1 + E[O_3](0)T}{E[O_3](0)T}\right).$$

In the limit of large T, $RB \to [H_2O](0)/[O_3](0)$. RB in this case is clearly a decreasing function of $[O_3](0)$ and reproduces the trend for RB shown in table VII. To estimate the explicit dependence of RB on $[O_3](0)$ for small T, substitute the approximation $(1 + (G/H)T)^{F/G} \approx 1 + (F/H)T$. In this case,

$$RB \approx \frac{[H_2O](0)}{[O_3](0)}\left(\frac{\big(B_2C_1ET\big)[O_3](0) + B_2C_1}{C_1E\big(B_2T + A_2\big)[O_3](0) + D_1D_2E}\right),$$

which is also a decreasing function of $[O_3](0)$ for each fixed T and reproduces the trend for RB shown in table VII.

5) Ozone depletion proceeds at a faster rate after sunrise in all three altitude intervals.

An analysis of this effect in terms of capture efficiencies was undertaken in subsect. **3**˙4. Estimates of pre- and post-sunrise capture efficiencies for two particle influx models are given in fig. 7. Larger post-sunrise capture efficiencies were attributed to a combination of photosensitivity of reaction rate coefficients β_1 through β_4, and differences in particle surface coverage by the primary adsorption monolayer.

H_2O_2 that escapes from particle surfaces before sunrise dissociates in sunlight. Liberated O combines with O_2 to recover O_3. H_2O_2 that escapes after sunrise suffers the same fate. This effect would tend to decrease ozone depletion rates. However, photo-excitation of O_3 and H_2O_2 at particle surfaces evidently increases the values of β_1 through β_4. A larger relative increase in β_1, for example, would tend to throttle the production of H_2O_2 and so increase net ozone depletion rates after sunrise.

Analysis of data in subsect. **2·7** suggests that bulk transport of air may occur above $19\,\mathrm{km}$ throughout winter. In this case, RH may be far less than 1.00 in the $24\,\mathrm{km}$ interval at the start of ozone hole formation. This possibility accounts for the virtual equality of pre- and post-sunrise capture efficiency estimates for the non-uniform particle influx model (fig. 7): the primary adsorption monolayer is not fully formed. At lower altitudes the primary monolayer is apparently fully formed both pre- and post-sunrise. The differences in capture efficiencies at these altitudes may be attributable to the differences in particle number densities and particle radii that figure in these calculations.

6) The overall percentage decrease in ozone number density is larger in the ozone layer ($\sim 70\%$ at $19\,\mathrm{km}$) than either above or below the ozone layer ($\sim 40\%$ at 24 and $14\,\mathrm{km}$).

This effect may be attributed to non-linearity in the unified system model presented in subsect. **3·6**. Although a complete analysis is beyond the scope of this paper, expression (36) for RD is suggestive. RD is evidently smallest at $19\,\mathrm{km}$ (table VII) because of contributions by several factors in the product $E[O_3](0)T = 2\beta_1(4\pi R^2\Theta)\cdot N(\varepsilon_{O_3} w_{O_3}/4\sigma_{O_3})^2[O_3](0)T$:

i) Θ is relatively small at $24\,\mathrm{km}$ because the primary monolayer is not fully formed. Thus, RD tends to be smaller at 19 and 14 than at $24\,\mathrm{km}$.

ii) N should be discounted at $24\,\mathrm{km}$. P_3 is the final phase of ozone hole formation. The stream that provided the influx of extraterrestrial particles may have passed before the end of P_3 and so the supply of particles to the $24\,\mathrm{km}$ interval may have diminished if not ceased. As number density decreases, the depletion rate also decreases.

iii) $[O_3](0)$ is largest at $19\,\mathrm{km}$, which tends to make RD smallest at $19\,\mathrm{km}$.

iv) The value of T should be discounted at $14\,\mathrm{km}$. Particles in any altitude interval during P_3 tend to be smaller, and so tend to have participated in ozone destruction longer. A side effect of this participation is loss of effectiveness (catalyst poisoning in heterogeneous catalysis [5]). As a result, equal or even larger numbers of these particles would be less effective in abetting the destruction of ozone at $14\,\mathrm{km}$.

7) The decline in ozone number density ceases at 24 and $14\,\mathrm{km}$ on about day 272; the decline at $19\,\mathrm{km}$ continues to day 280 at least.

We suggest that ozone destruction ceases in the $24\,\mathrm{km}$ interval, possibly by day 265, because of decreased particle number density and critically low values of relative humidity. The decrease in particle number density would be due to diminished influx. Combinations of temperature and water vapor density corresponding to $RH \approx 0.18$ (table X) may even drive desorption of the primary monolayer. The final value of ozone number density is about $2.4 \times 10^{12}\,\mathrm{cm}^{-3}$.

We suggest that ozone destruction ceases in the 19 and $14\,\mathrm{km}$ intervals because of diminished particle influx and catalyst poisoning during prolonged exposure of particle

surfaces to ozone depletion reactions. According to fig. 5, the final value for ozone number density is about $1.4 \times 10^{12} \, \text{cm}^{-3}$ for both altitude intervals. The corresponding curves may even approach their final values about the same time.

These observations support the view that ozone destruction ceases because of a critical decrease in particle number density or a critical decrease in catalytic efficiency through poisoning or desorption of the primary monolayer.

3˙8. *Conclusions*. – Analysis of data for the year 1986 supports the circumpolar vortex theory. Air infiltrates the South Polar Region at and above the ozone layer during sunset and early winter. As the vortex forms, air in the ozone layer stabilizes and evidently remains stable through the formation of the ozone hole. The altitude of the ozone layer may fluctuate but the air mass itself remains constant. Transport may occur above the ozone layer during winter but the effects of mixing at its upper boundary are evidently marginal.

Decreasing temperatures during sunset and winter increase relative humidity until ambient aerosols are activated as ice-forming nuclei. As temperatures continue to fall, these particles convert water vapor in excess of saturation to ice. These ice crystals then depart the ozone layer under the influence of gravity. By the start of ozone hole formation, the ozone layer is likely to have exceptionally low ambient aerosol counts and water vapor density near saturation. Increasing temperatures during ozone hole formation produce conditions of sub-saturation preventing ice crystal formation.

The chemistry governing the evolution of $[\text{O}]$ and $[\text{O}_3]$ in the gas phase during sunset and winter is evidently well understood and unrelated to the formation of the ozone hole. This paper has presented a derivation of the evolution equations, the solution for the ozone layer over South Pole during sunset and winter, and comparison of predictions and measurements for 1986. Measured changes in $[\text{O}_3]$ in the ozone layer during this period can easily be attributed to transport. Without the influence of some additional agent, O_3 is effectively a stable atmospheric constituent and its concentration should remain constant through sunrise.

Part I of this paper provided an analysis of magnetic spherules collected in an extended program of atmospheric sampling. This analysis showed that the source of these spherules is a major stream of extraterrestrial particles independent of known meteor showers. This analysis also yielded a general quantitative theory relating magnetic spherule measurements at ground level and extraterrestrial particle number densities at the altitude of the ozone layer. Applying this theory to specific spherule measurements, we project that this stream provides particles at the ozone layer over South Pole precisely at ozone hole formation and that the concentration of these particles lies between 500 and $2000 \, \text{m}^{-3}$.

We have hypothesized that the ozone hole is formed by the destruction of ozone at extraterrestrial particle surfaces. We have tested this hypothesis in two steps. The first was to construct a unified mathematical model of ozone depletion based on analysis of

   i) the evolution of the size distribution of extraterrestrial particles in the ozone layer,

  ii) transport of ozone to particle surfaces by diffusion,

 iii) chemical and physical adsorption at particle surfaces,

 iv) a simple system of chemical reactions involving ozone destruction at particle surfaces.

The model took the form of a system of equations expressing the evolution of $[O_3]$ in terms of diffusion, adsorption, and reaction rates at particle surfaces.

The second step in testing this hypothesis was to assess the extent to which the unified model accounts for the observed features in ozone hole formation. These features include

i) the simultaneous onset of ozone hole formation at 14, 19, and 24 km three weeks before sunrise,

ii) the non-linear dependence of $[O_3](t)$ on $[O_3](0)$, its value at the start of ozone hole formation,

iii) the spike in $[O_3]$ at 14, 19, and 24 km at sunrise,

iv) the non-linear dependence of the magnitude of the spike on $[O_3](0)$,

v) the resumption of a more rapid decline in $[O_3]$ after sunrise,

vi) the dependence of overall percentage decrease in ozone number density on altitude,

vii) the cessation in the decline in $[O_3]$ before disintegration of the circumpolar vortex.

Analysis shows that the unified model accounts for each of these features.

The continuous observation of ozone concentration beginning in the late fifties by the British Antarctic Survey has shown that the ozone hole first formed as early as 1968. Studies of radioactivity associated with aerosol particles by the author in the mid and late fifties show a virtual absence of magnetic spherules in particle samples. However, atmospheric sampling in 1967, 1969, and 1971 in subsequent studies of Bowen's Hypothesis shows an abundance of magnetic spherules [1]. This coincidence lends credence to the extraterrestrial particle theory of ozone hole formation. Evidently, within the time frame of the British observations, the Earth's orbit first transected the extraterrestrial particle stream some time in the mid sixties and has transacted it annually since. Further, the Earth's orbit may actually transect this stream twice each year: once beginning in August and ending in October with particle influx primarily in the southern hemisphere, and once six months later with particle influx primarily in the northern hemisphere. The northern influx would be responsible for ozone hole formation over North Pole (fig. 8, [17]).

Conclusion: Analysis of data has developed strong evidence that the ozone hole is primarily a natural phenomenon caused by the depletion of ozone in reactions on the surfaces of extraterrestrial particles.

* * *

APPENDIX A.

Sunrise and sunset

Recall that the ozone layer over South Pole sees only semi-annual alternations in sunlight and shadow. The object of this appendix is to estimate the days of the year on which these alternations occur.
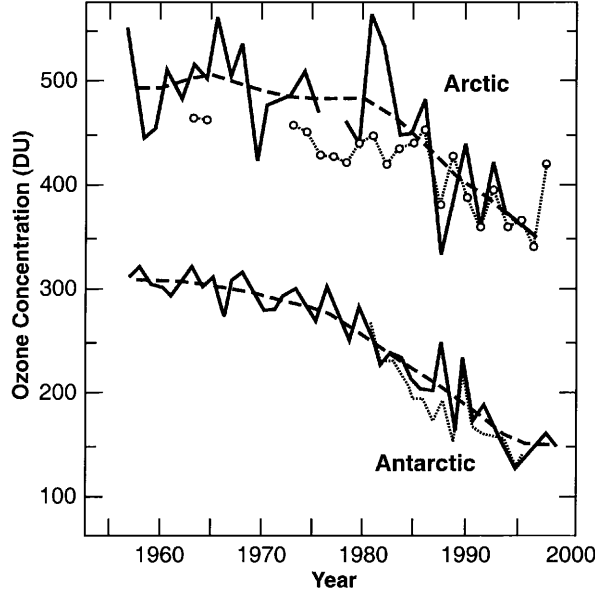
Fig. 8. – Ozone concentration *vs.* year for Arctic and Antarctic Polar Regions.

Solar declination is given by [18]

$$\delta = 23.45 \sin\left(2\pi\frac{284 + d}{365}\right),$$

where

δ is the solar declination, angular position of the sun at solar noon with respect to the plane of the equator ($°$),

d is the day of the year.

Estimates of the days of the year on which an observer over South Pole at $19\,\mathrm{km}$ (ozone layer) sees first and last direct sunlight are obtained by solving this equation for d, where $\delta \equiv \delta_1 + \delta_2 + \delta_3$. These terms represent contributions to δ based on the radius of the sun, the altitude of the ozone layer, and atmospheric refraction of sunlight.

Radius of the sun: The distance between the Earth and the sun is $\sim 150 \times 10^6\,\mathrm{km}$ and the diameter of the sun is $\sim 1.39 \times 10^6\,\mathrm{km}$, so the solar angle is $(1.39/150) \times 360 \approx 3.34°$ and the solar half-angle is $\delta_1 \approx 1.67°$.

Altitude of the ozone layer: Consider the ray shown in fig. 9 that originates in the ozone layer over South Pole and is tangent to the Earth. R denotes the radius of the Earth ($12714\,\mathrm{km}$) and h denotes the altitude of the ozone layer (km). The point of origin is $(0, -(R+h))$ and the point of tangency is $(R\cos\phi, -R\sin\phi)$. Without refraction, an observer at the point of origin would first see direct sunlight when the sun is $\pi/2 - \phi$ (radians) below the horizon relative to an observer on the ground at South Pole. The relation $\cos(\pi/2 - \phi) = R/(R + h)$ is apparent in the figure. We take the value of R to be $5.4\,\mathrm{km}$ greater than the radius of the Earth at sea level ($2.7\,\mathrm{km}$ to account for the altitude of the East Antarctic plateau and $2.7\,\mathrm{km}$ to account for the thickness of
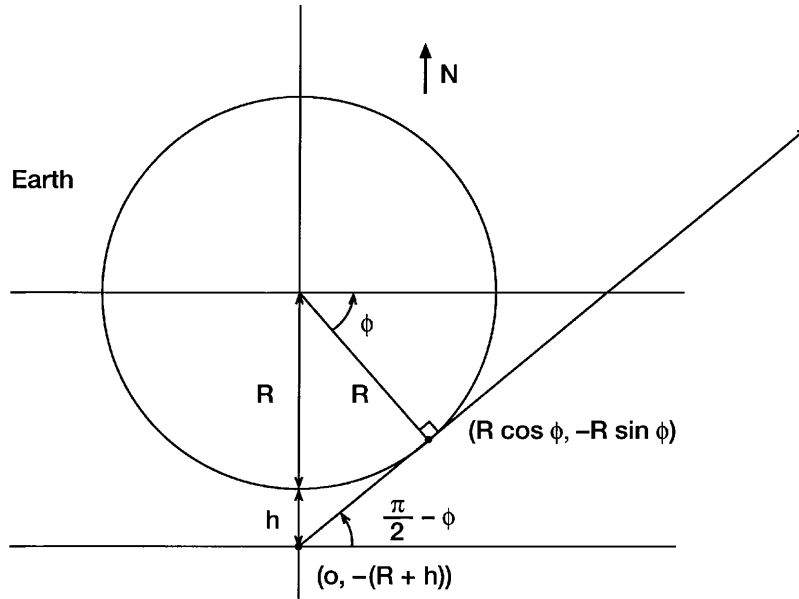
Fig. 9. – A diagram depicting a ray originating h km above South Pole and tangent to the Earth.

continental ice cap). The corresponding value of h is $19 - 5.4 = 13.6$ km. In this case, $\delta_2 = (360/2\pi)\cos^{-1}(R/(R+h)) \approx 2.65°$.

Atmospheric refraction of sunlight: Consider the thin-shell model of the atmosphere depicted in fig. 10. n_1 and n_2 denote the indices of refraction for the shells between radii r_0 and r_2, θ_1 and θ_2 denote angles of incidence for a ray of light at radii r_1 and r_2, and ξ_1 denotes angle of refraction corresponding to θ_1. Snell's Law implies $n_1 \sin\theta_1 \approx n_2 \sin\xi_1$. The law of sines implies $r_2 \sin\theta_2 = r_1 \sin\xi_1$. Taken together, these relations imply $r_1 n_1 \sin\theta_1 \approx r_2 n_2 \sin\theta_2$. In the limit of very thin shells, we have that light follows trajectories characterized by the relation $r \cdot n(r) \cdot \sin\theta = \text{const}$. The value of the constant is $R \cdot n(R)$ for trajectories tangent to the Earth.

θ also satisfies $\mathrm{d}r \propto \cos\theta$ and $r \cdot \mathrm{d}\phi \propto \sin\theta$, where r and ϕ denote polar coordinates of a point on such a trajectory. Consequently,

$$\frac{1}{r}\frac{\mathrm{d}r}{\mathrm{d}\phi} = \frac{\cos\theta}{\sin\theta} = \left(\frac{1}{\sin^2\theta} - 1\right)^{1/2}.$$

Substituting for $\sin\theta$,

$$\mathrm{d}\phi = \left(\left(\frac{r \cdot n(r)}{R \cdot n(R)}\right)^2 - 1\right)^{-1/2}\frac{\mathrm{d}r}{r}.$$

For clarity, take $(0, R)$ to be the point of tangency. Then

$$\phi = \pi/2 + \int_1^{r/R} \frac{\mathrm{d}s}{s\left(s^2 N(s) - 1\right)^{1/2}},$$
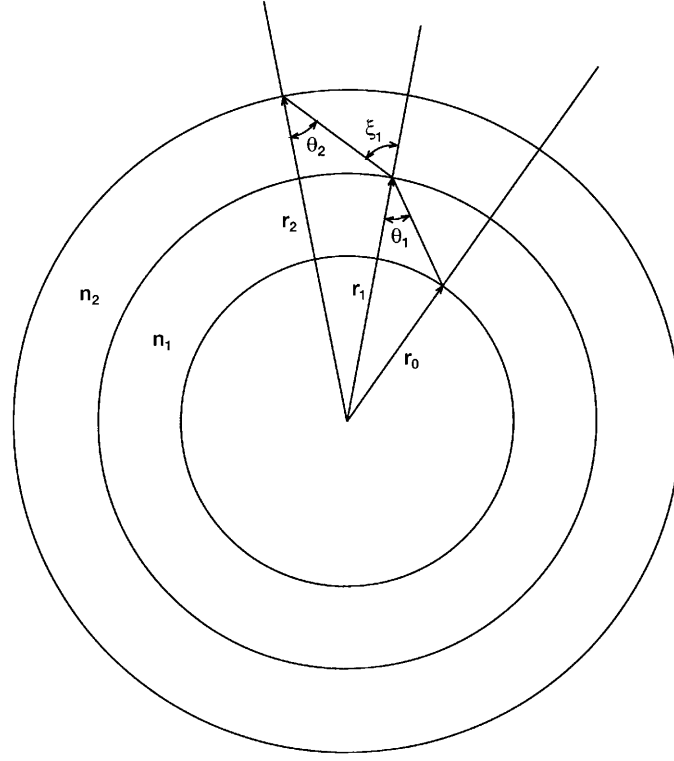
Fig. 10. – A diagram depicting two shells in a thin-shell model of refraction in the atmosphere. n_1 and n_2 denote indices of refraction, θ_1 and θ_2 denote angles of incidence for a ray of light at radii r_1 and r_2, and ξ_1 denotes the angle of refraction corresponding to θ_1.

where $N(s) \equiv (n(Rs)/n(R))^2$.

Figure 11 depicts the trajectory tangent at $(0, R)$. $\pi/2 + \mu$ denotes the polar coordinate of an observer on this trajectory at altitude h. Without refraction, the observer would first see direct sunlight when the sun is η (radians) below the horizon relative to an observer on the same radius at ground level. Refraction between the observer and the point of tangency is given by the integral $I(h/R)$:

$$I\frac{h}{R} = \mu - \eta = \int_1^{1+h/R} \frac{\mathrm{d}s}{s\left(s^2 N(s) - 1\right)^{1/2}} - \cos^{-1}\left(\frac{R}{R+h}\right)$$

$$= \int_1^{1+h/R} \left(\left(\frac{s^2 - 1}{s^2 N(s) - 1}\right)^{1/2} - 1\right) \frac{\mathrm{d}s}{s\left(s^2 - 1\right)^{1/2}}.$$

To evaluate $N(s)$, note that in general $n = \sqrt{K_\mathrm{m} \cdot K_\mathrm{e}}$, where K_m denotes relative permeability and K_e denotes dielectric constant [19]. $K_\mathrm{m} \approx 1.0$ and $K_\mathrm{e} \approx 1 + a\rho(r)$ for air, where $a \approx 5.9 \times 10^{-4}\,\mathrm{atm}^{-1}$ and ρ denotes air density (in atmospheres). To satisfactory
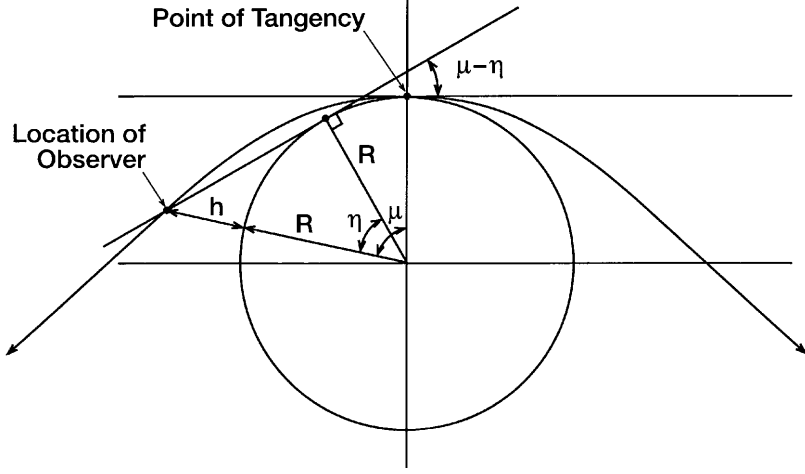
Fig. 11. – A diagram depicting the optical trajectory tangent to the Earth at the point $(0, R)$. $\pi/2 + \mu$ denotes the polar coordinate of an observer on this trajectory at altitude h. Without refraction, the observer would first see direct sunlight when the sun is η (radians) below the horizon relative to an observer on the same radius at ground level.

approximation, $\rho(r) = \rho(R) \cdot \exp[-b(r - R)]$, where $b \approx 1/6.7 \, \text{km}^{-1}$ [4]. Then,

$$N(s) \approx \frac{1 + a \cdot \rho(R) \cdot \exp\left[-bR(s - 1)\right]}{1 + a \cdot \rho(R)}.$$

We have applied these considerations to the case in which an observer at $19 \, \text{km}$ first sees the leading edge of the rising sun. We have taken $R = 12719.4 \, \text{km}$ and $h = 13.6 \, \text{km}$. In this case, $\rho(R) \approx 0.447$. Finally, Φ_3 is the sum of the refractions between the observer and the point of tangency, and between the point of tangency and the sun: $\delta_3 = (360/2\pi) \cdot (I(h/R) + I(\infty)) \approx 0.29° + 0.45° = 0.74°$.

To find the days of first and last direct sunlight we solve the declination equation with $\delta \equiv \delta_1 + \delta_2 + \delta_3 = 5.06°$. We estimate that for an observer at $19 \, \text{km}$ altitude at South Pole, the last day of direct sunlight is April 4 (day 94, sunset), and the first day of direct sunlight is September 8 (day 251, sunrise). We have repeated this exercise to include a $3 \, \text{km}$ thick cloud cover ($R = 12722.4 \, \text{km}$ and $h = 10.6 \, \text{km}$). In this case, the last day of direct sunlight at sunset is April 2, and the first day of direct sunlight at sunrise is September 10.

APPENDIX B.

Diffusion of ozone

The object of this appendix is to derive a differential equation for the evolution of ozone number density in terms of particle number density, radius, and ozone capture efficiency. The point of particular interest is the derivation of a modified diffusion coefficient for ozone in air that extends the Brownian diffusion theory to the kinetic regime.

The diffusion equation for ozone near an isolated particle is given by [20]

(B.1)
$$\frac{\partial C}{\partial t} + \vec{u} \cdot \nabla C = D \nabla^2 C,$$

where

C is the ozone number density ($\#/\text{cm}^3$),

t is the time (s),

$\vec{u}$ is the flow field of air past the particle (cm/s),

D is the diffusion coefficient (cm^2/s).

The Einstein relation $\langle r^2 \rangle = 2Dt$ gives r.m.s. displacement of an ozone molecule in air as a function of time [10]. In this sense, the time for a molecule to migrate a distance equal to the radius of a particle is $t = R^2/2D$. The distance d the particle falls at terminal velocity v in this time is $d = vt = (Rv/2D)R$. Substituting typical values $R \sim 10^{-3}\,\text{cm}$, $v \sim 1\,\text{cm/s}$, and $D \sim 0.5\,\text{cm}^2/\text{s}$, we estimate that $d \sim 10^{-3}R$, *i.e.*, ozone tends toward its equilibrium distribution about the particle on the order of 10^3 times faster than the particle perturbs this distribution as it falls through air at terminal velocity. Thus, the contribution of the diffusion term in eq. (B.1) is dominant and we adopt the approximation

(B.2)
$$\nabla^2 C = 0.$$

Let ε denote capture efficiency, the probability that a collision between an ozone molecule and a particle results in the capture of the molecule by the particle. Let C_∞ denote ozone number density far from the particle. Then the solution of eq. (B.2) that satisfies these boundary conditions is

$$C(r) = C_\infty \left(1 - \varepsilon \frac{R}{r} \right),$$

where we assume the particle is spherical and the origin of the coordinate system is located at its center. According to elementary diffusion theory, the ozone capture rate Γ_D ($\#/\text{particle/s}$) is the product of the particle surface area, the ozone diffusion coefficient, and the ozone number density gradient at the particle surface:

(B.3)
$$\Gamma_D = \left(4\pi R^2 \right) D \frac{\partial C}{\partial r}(R) = 4\pi \varepsilon C_\infty D R.$$

Kinetic theory provides the expression $D = \pi w \lambda / 8$, where w denotes the average speed of an ozone molecule and λ denotes mean free path [10]. Substituting,

$$\Gamma_D = \pi^3 \varepsilon C_\infty w \lambda R / 2.$$

Since λ is inversely proportional to the density of air, this theory clearly fails in the limit of a rarified atmosphere. An arbitrarily large mean free path cannot produce an arbitrarily large capture rate.

To derive a more appropriate expression for D, we consider a spherical control volume of radius R_∞ centered at the origin, and an ozone molecule executing a random walk

based on molecular collisions. Let $P(\lambda, R, R_\infty)$ denote the probability that once the molecule enters the control volume, it then collides with the particle before exiting the control volume. P is easily obtained by computer simulation. In general,

$$P(\lambda, R, R_\infty) = \left(\frac{R}{R_\infty}\right)^2 \chi \frac{\lambda}{R}$$

with numerical estimate

$$\chi(x) \cong \frac{x}{x + 2/\pi} + \alpha x^{\beta+1} e^{-\gamma x},$$

where $\alpha = 0.1388$, $\beta = 0.1180$, $\gamma = 0.5172$. Let S denote the rate at which ozone molecules cross a hypothetical plane ($\#/\mathrm{cm}^2/\mathrm{s}$) in a homogeneous gas. Kinetic theory provides the expression $S = C_\infty w/4$ [10]. A corresponding kinetic theoretic estimate for the ozone capture rate is

$$\Gamma_\mathrm{K} = 4\pi R_\infty^2 S P(\lambda, R, R_\infty)\varepsilon = \pi\varepsilon C_\infty w R^2 \chi \frac{\lambda}{R}.$$

By equating the diffusion and kinetic capture rates, we obtain an expression for a generalized Brownian diffusion coefficient D^* that accounts for the bound on capture rate imposed by kinetic theory:

$$D^* = wR\chi(\lambda/R)/4.$$

A more rigorous treatment of D^* is beyond the scope of this paper.

Finally, the depletion rate of ozone ($\#/\mathrm{cm}^3/\mathrm{s}$) due to capture by particles is just Γ_{D^*} times particle number density N ($\#/\mathrm{cm}^3$). According to eq. (B.3),

$$\frac{\mathrm{d}}{\mathrm{d}t}[\mathrm{O}_3] = -4\pi\varepsilon D^* RN[\mathrm{O}_3].$$

REFERENCES

[1] ROSINSKI J. and KERRIGAN T. C., *The Role of Extraterrestrial Particles in the Formation of the Ozone Hole, Part I: The Concentration of Extraterrestrial Particles at Ozone Hole Formation*, Nuovo Cimento C, **24** (2001) 815.
[2] DANILOV A. D., *Chemistry of the Ionosphere* (Plenum Press, New York, N. Y.) 1970.
[3] FLEAGLE R. G. and BUSINGER J. A., *An Introduction to Atmospheric Physics* (Academic Press, New York, N. Y.) 1963.
[4] *Handbook of Geophysics* (Macmillan, New York, N. Y.) 1961.
[5] BARROW G. M., *Physical Chemistry* (McGraw-Hill, New York, N. Y.) 1979.
[6] KOMHYR W. D., OLTSMAN S. J. and GRASS R. D., *J. Geophys. Res.*, **93** (1988) 5167.
[7] RATCLIFFE J. A. (Editor), *Physics of the Upper Atmosphere* (Academic Press, London) 1962.
[8] REES M. H., *Physics and Chemistry of the Upper Atmosphere* (Cambridge University Press, Cambridge, Great Britain) 1989.
[9] LEIGHTON R. B., *Principles of Modern Physics* (McGraw-Hill, New York, N. Y.) 1959.
[10] REIF F., *Fundamentals of Statistical and Thermal Physics* (McGraw-Hill, New York, N. Y.) 1965.

[11] FUCHS N. A., *The Mechanics of Aerosols* (Macmillan, New York, N. Y.) 1964.
[12] PAULING L., *General Chemistry* (Dover, New York, N. Y.) 1970.
[13] SENNETT P. and OLIVER J. P., *Colloidal dispersions, electrokinetic effects, and the concept of the zeta potential*, in *Chemistry and Physics of Interfaces* (American Chemical Society, Washington D. C.) 1965.
[14] DEITZ V. R., *Gas adsorption. The extreme limits of surface coverage*, in *Chemistry and Physics of Interfaces* (American Chemical Society, Washington D. C.) 1965.
[15] HUDSON J. B. and ROSS S., *Adsorption and condensation processes*, in *Chemistry and Physics of Interfaces* (American Chemical Society, Washington D. C.) 1965.
[16] DACEY J. R., *Surface diffusion of adsorbed molecules*, in *Chemistry and Physics of Interfaces* (American Chemical Society, Washington D. C.) 1965.
[17] RASMUSSEN C. (Editor), *Ozone Update, UCAR Quarterly*, Vol. **27**, (1998).
[18] DUFFIE J. A. and BECKMAN W. A., *Solar Energy Thermal Processes* (Wiley, New York, N. Y.) 1974.
[19] REITZ J. R. and MILFORD F. J., *Foundations of Electromagnetic Theory* (Addison-Wesley, Reading, Massachusetts) 1967.
[20] BATCHELOR G. K., *An Introduction to Fluid Dynamics* (Cambridge University Press, New York, N. Y.) 1967.